SINGLE CELLS

ORGANIZED MULTICELLS

SUPERCELLS

FIG. 2. Typical wind hodographs for (a) single cell storms and disorganized multicell storms producing only sporadic bursts of hail, (b) well-organized multicell hailstorms, and (c) supercell hailstorms. The supercell hodograph is similar to the multicell case but exhibits stronger directional shear at low levels. (From Chisholm and Renick, 1972.)

CLOUD BASE

$\overline{V}_c$

12 km (MSL)

CLASS III

$\overline{V}_c$

CLOUD BASE
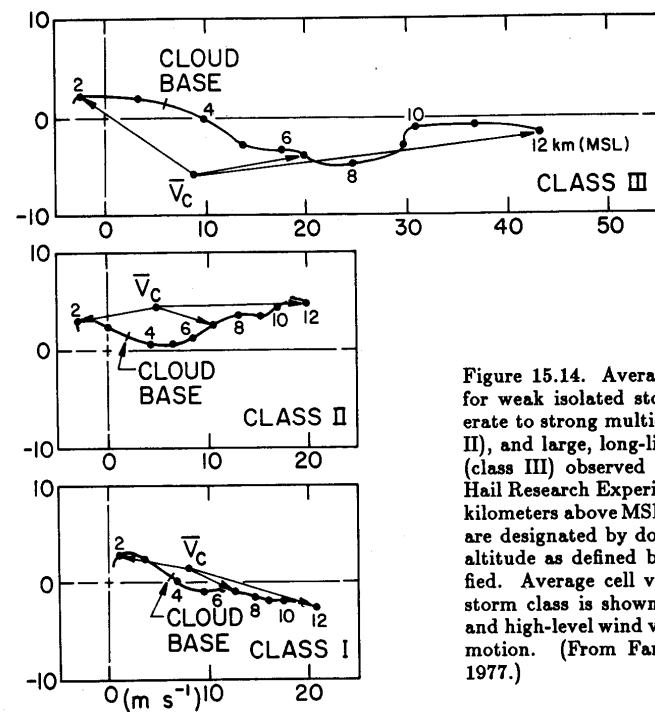
CLASS II

$\overline{V}_c$

CLOUD BASE   CLASS I

Figure 15.14. Average wind hodographs for weak isolated storms (class I), moderate to strong multicellular storms (class II), and large, long-lived supercell storms (class III) observed during the National Hail Research Experiment. Heights are in kilometers above MSL; increments of 1 km are designated by dots. Mean cloud base altitude as defined by the LCL is identified. Average cell velocity, $\overline{V}_c$, for each storm class is shown with low-, middle-, and high-level wind vectors relative to cell motion. (From Fankhauser and Mohr, 1977.)

NHRE

ALBERTA HAIL PROJECT

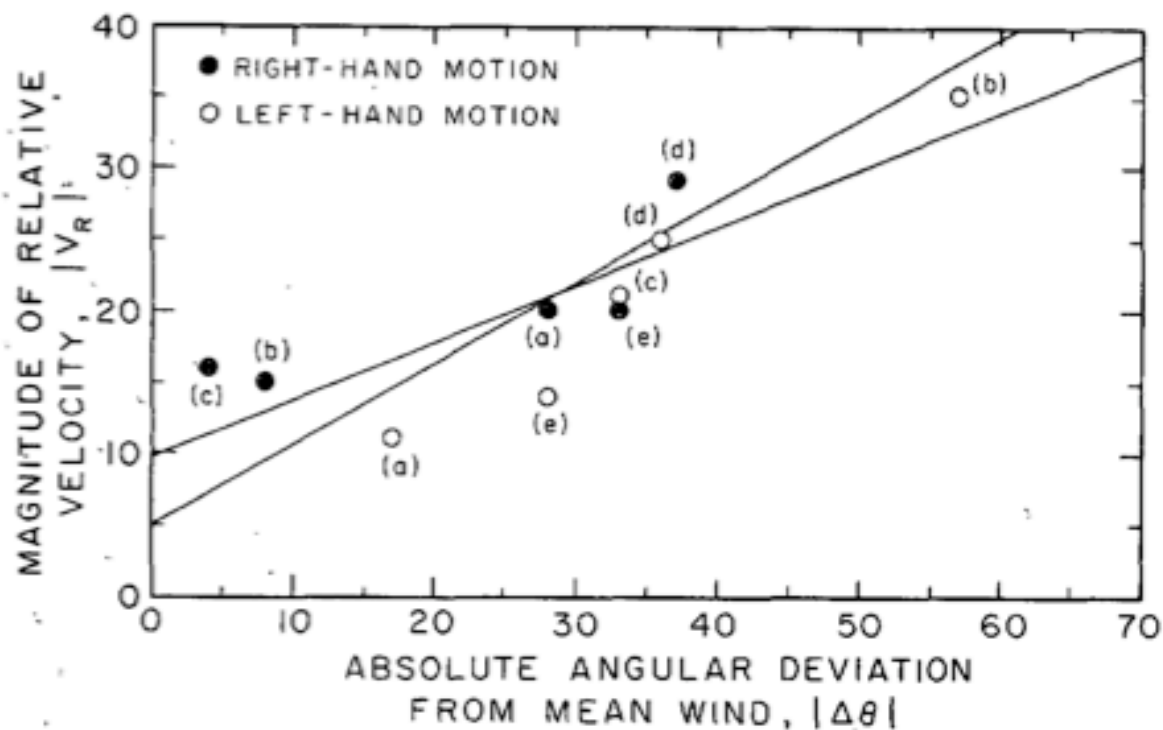CELL MOTION, PROPAGATION (DISCRETE, CONTINUOUS), AND STORM MOTION

FIGURE 23.—Scatter diagram and regression lines showing the relationship between magnitude of the relative wind and angular deviation of the radar echo path from the mean wind direction. The data were taken from the cases shown in figure 20: (a) May 24, 1962 (Newton and Fankhauser 1964); (b) Apr. 3, 1964 (Fujita and Grandoso 1968, Charba and Sasaki 1968); (c) Apr. 23, 1964 (Hammond 1967, Fujita and Grandoso 1968); (d) May 27, 1965 (Harrold 1966); and (e) June 1, 1965 (case I, sec. 2).
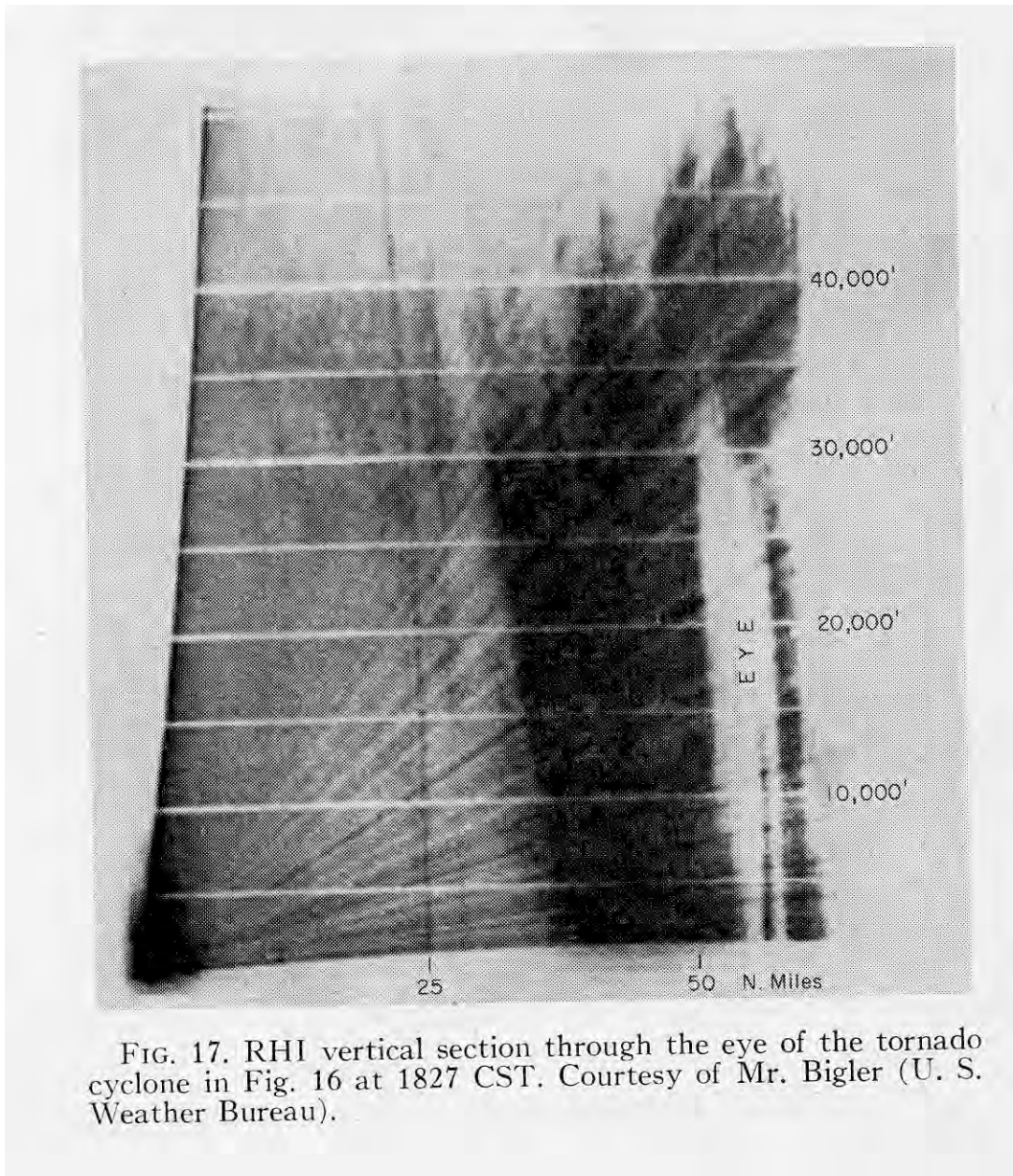
Fankhauser 1971

FIG. 17. RHI vertical section through the eye of the tornado cyclone in Fig. 16 at 1827 CST. Courtesy of Mr. Bigler (U. S. Weather Bureau).

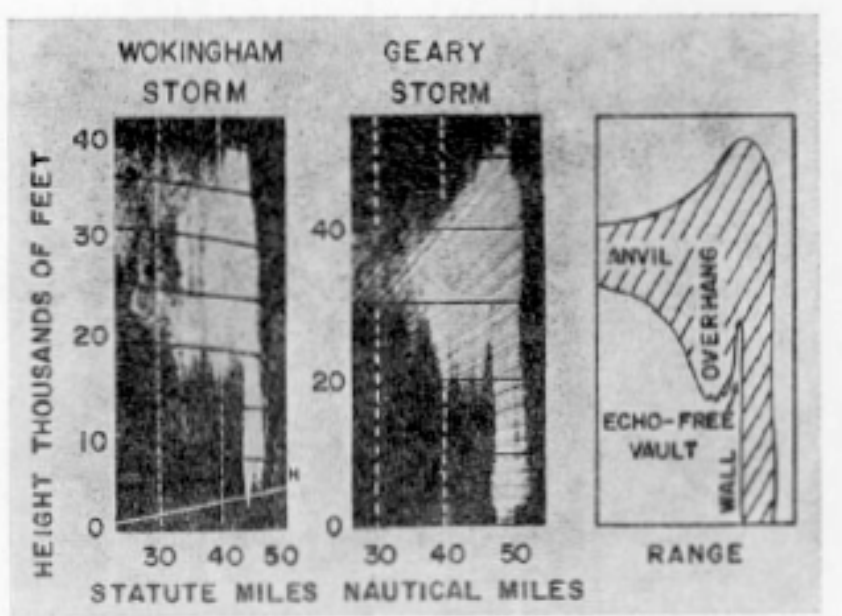Fujita (1963)   22 April 1958   Texas A&M

FIG. 5. Full gain RHI photographs illustrating the similarity of the structure of the Wokingham and Geary storms during their most intense phases. Storm motion in both photographs is *from right to left*. The photograph of the Geary storm was obtained from the 10 cm FPS-6 radar at 1756½ CST on 291 degrees. The photograph of the Wokingham storm was obtained using a 3.3 cm AN/TPS-10 radar [reproduced from Fig. 42 of Browning and Ludlam, 1960: *Radar analysis of a hailstorm*. Tech. Note No. 5. Contract AF61(052)-254, Dept. of Meteor., Imperial College, London]. The rear edge of the latter is severely attenuated: however the overhang, the (admittedly rather shallow) vault, and the wall are seen largely unattenuated.

Browning and Ludlam 1962
Browning and Donaldson 1963

Vault, WER, BWER, echo-free hole

- IN BETWEEN CELLS
* • STRONG UPDRAFT
- DOWNDRAFT
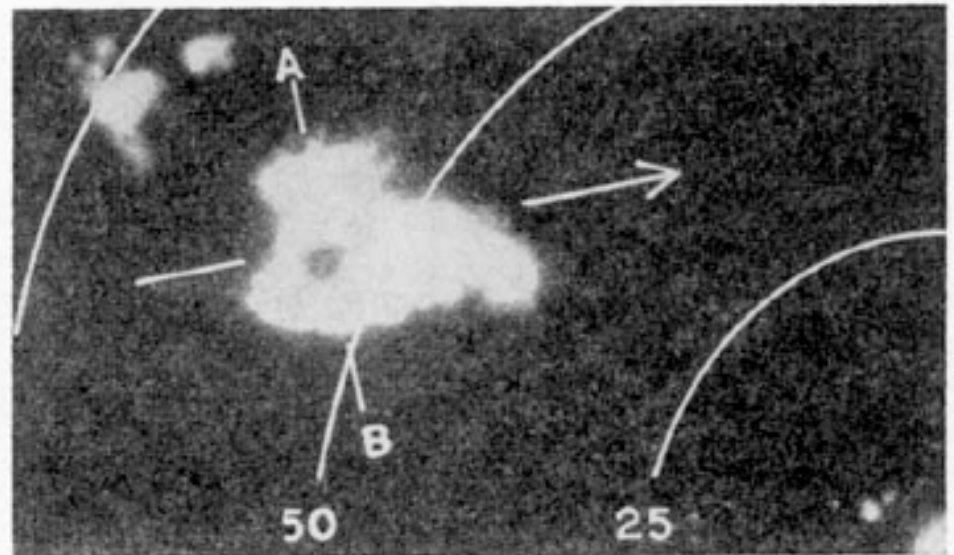- CENTRIFUGING OF PARTICLES (Ligda et al. 1957)

FIG. 10. Photograph at 1747 CST of part of the CPS-9 PPI-scope 20 db below full sensitivity at 4° elevation, showing the vault as a totally enclosed echo-free hole. The arrow gives the storm's direction of travel and AB gives the orientation of Fig. 9.
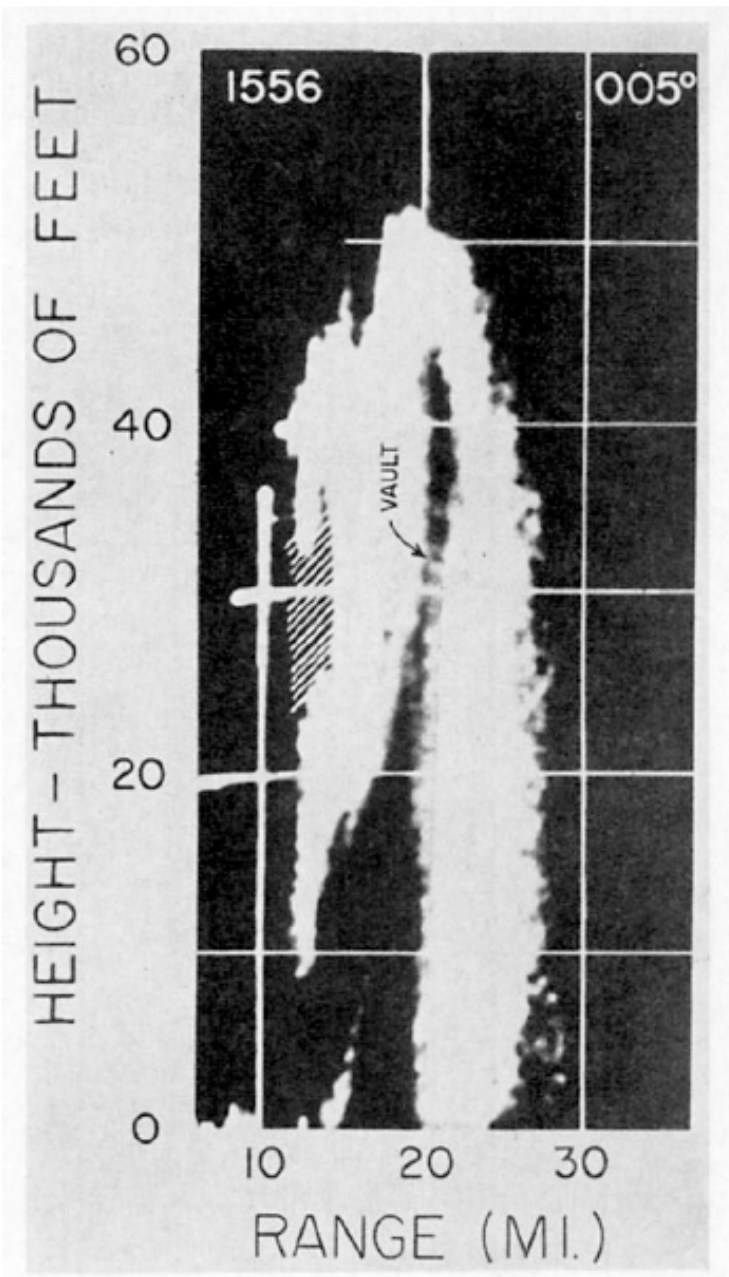
FIG. 7a. Vertical section through Storm E and the curtain obtained with the FPS-6 along 005 deg at 1556 CST. Fig. 7a shows an original RHI photograph with exaggerated vertical scale for which $Z_e = 10^4$ mm^6 m^{-3} at 20 mi range.
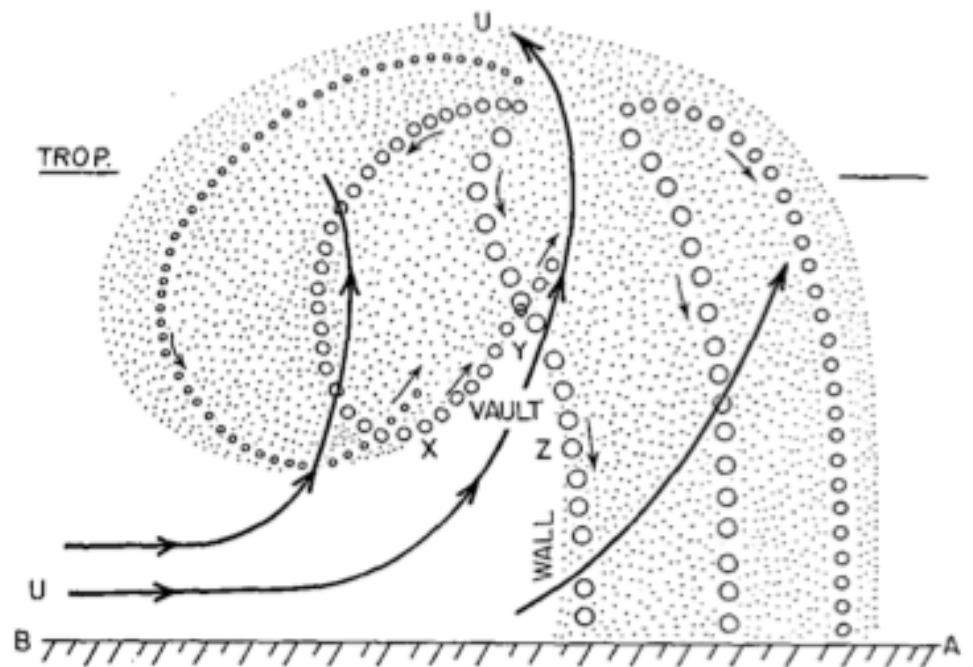
FIG. 9. Vertical section showing schematically how a vault might be produced within an intense updraft. Solid lines are streamlines of airflow within the updraft, the updraft axis being along UU. Circles represent hailstone trajectories, the size of the circles denoting whether the stones are small, medium or large. The stippled area denotes the approximate extent of echo (Z_e about 10^3 mm^6 m^{-3}). The orientation AB corresponds to that in Fig. 5 of Browning (1964).
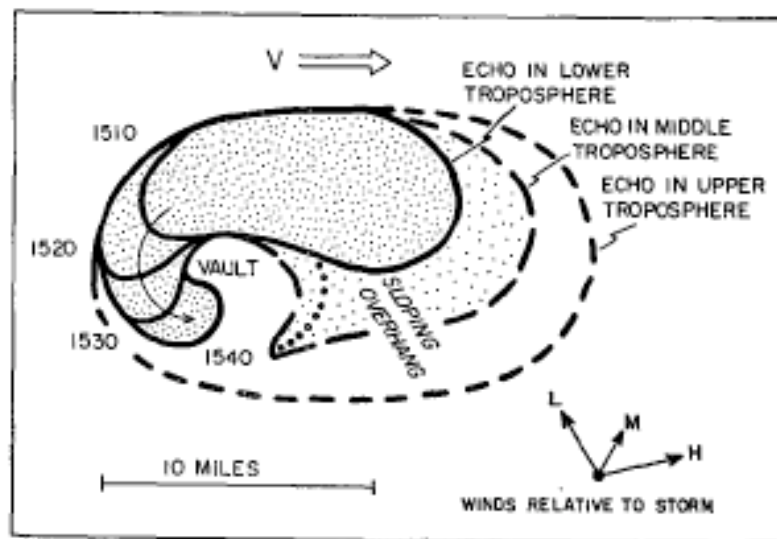
Browning 1965a

FIG. 2. Schematic diagram illustrating the development of the hook echo within Storm E, successive positions of the hook being shown at times 1510, 1520, 1530 and 1540 CST.
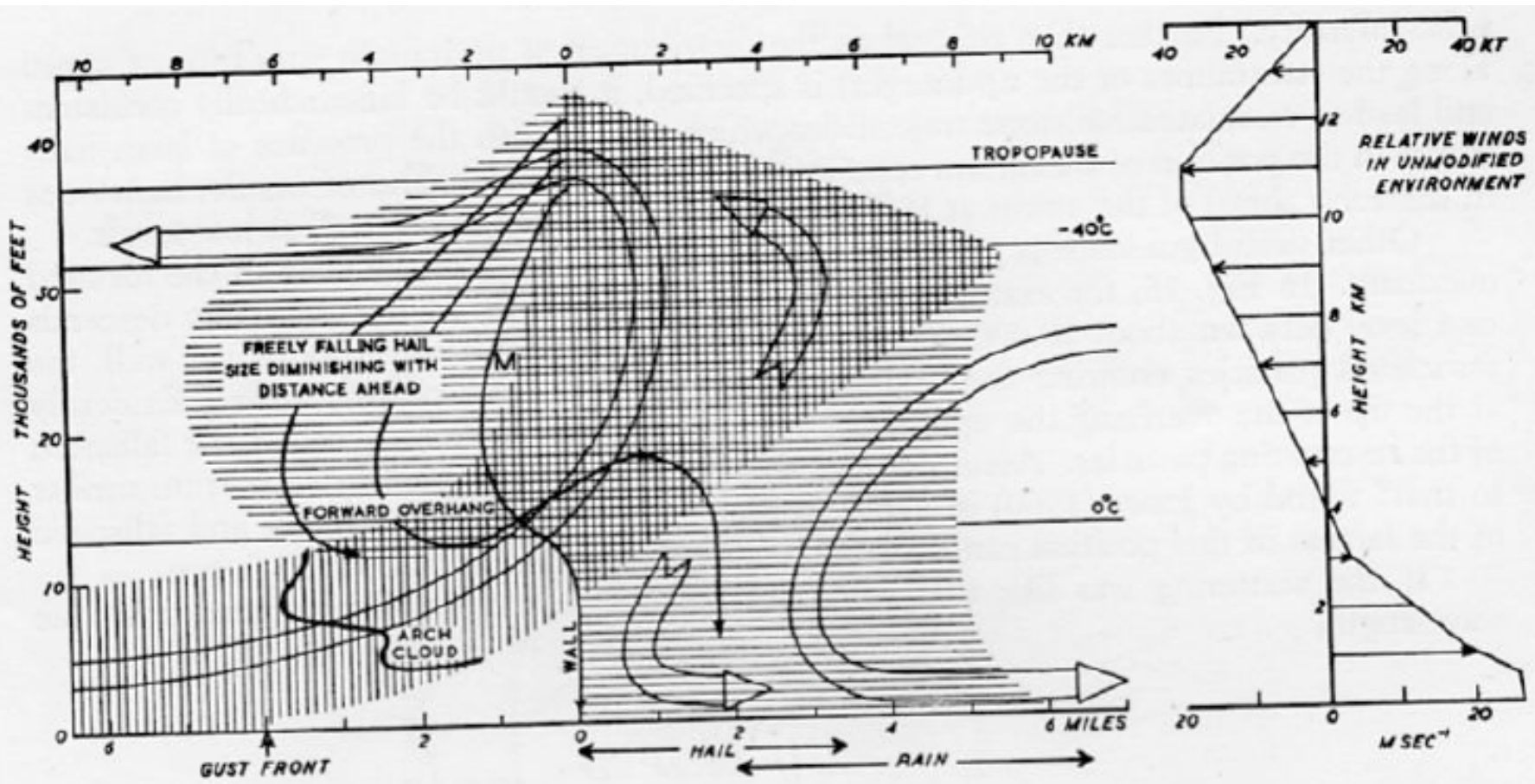
Browning 1965

Figure 16. Vertical section through the centre of the storm along the direction of motion (from right to left of the diagram). The extent of the updraught is denoted by vertical hatching and that of echo whose intensity Z_e exceeds 10^3 mm^6 m^{-3} is denoted by horizontal hatching. Some hailstone trajectories are indicated.

Browning and Ludlam 1962
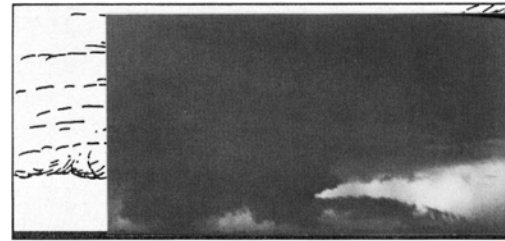
Formation of Fargo Tornado
beneath a
Mesocyclone (rotating) Cloud
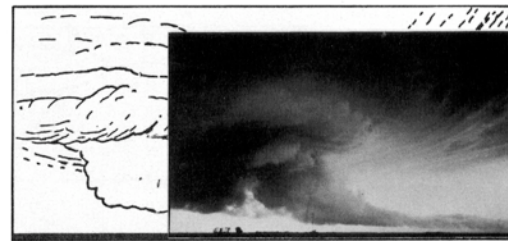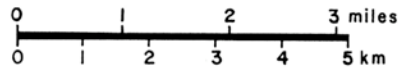
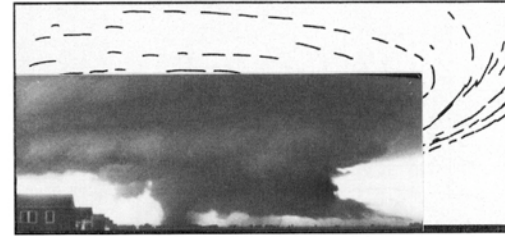1820 CST   266°   3.3 mi   10C

1814 CST   269°   6.4 mi   09A

1831 CST   278°   7.1 mi   43D
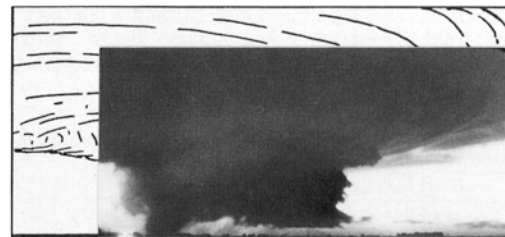
1816 CST   268°   5.8 mi   09B

1834 CST   279°   6.4 mi   43E

1817 CST   296°   6.1 mi   29A

1837 CST   280°   5.4 mi   43F

"WALL CLOUD"
"TAIL CLOUD"

Fig. 2.2-4 Evolution of the parent cloud of the Fargo tornado. At 1815 CST, 12 min before the tornado formation, the cloud was characterized by a small but well-defined wall cloud and a long tail cloud to the right (north). After touchdown, the tornado axis tilted, pushing the tornado on the surface directly beneath the south edge of the wall cloud.

Fujita (1959) 20 June 1957
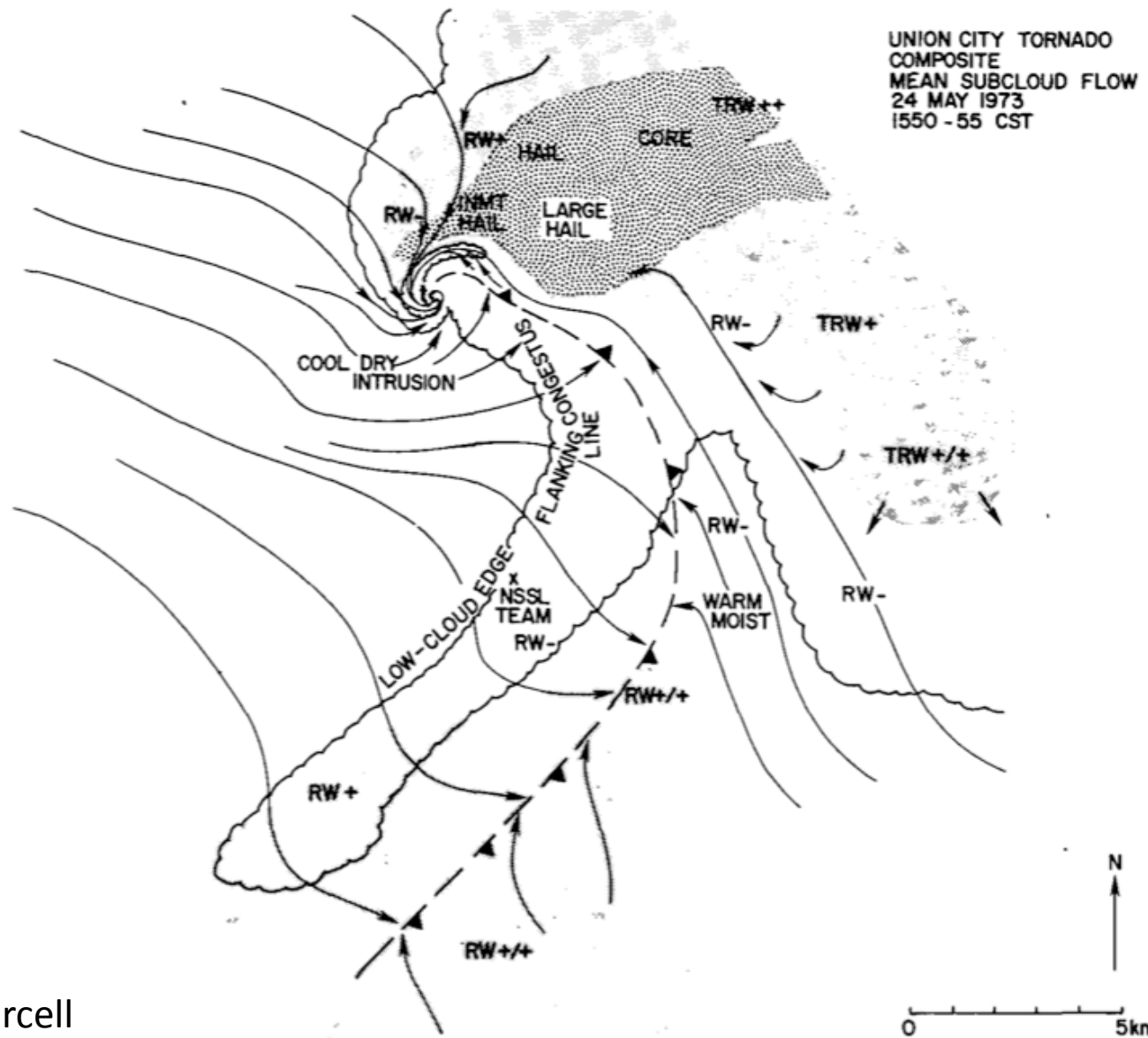
Golden and Purcell 1978

FIG. 8. Schematic plan view of composited mean subcloud mesoscale flow around Union City tornado (at **t**) during mature stage. Surface gust-front location is dashed, major low-level cloud boundaries, precipitation types and intensities are indicated. Regions of heavier precipitation are shaded. Note flanking line of cumulus congestus located (scalloped cloud-base boundaries) relative to surface gust front, streamflow and tornado. Tornado structure during this compositing period as in Fig. 7. Southern rainshower area was primarily associated with middle cloud at this stage.
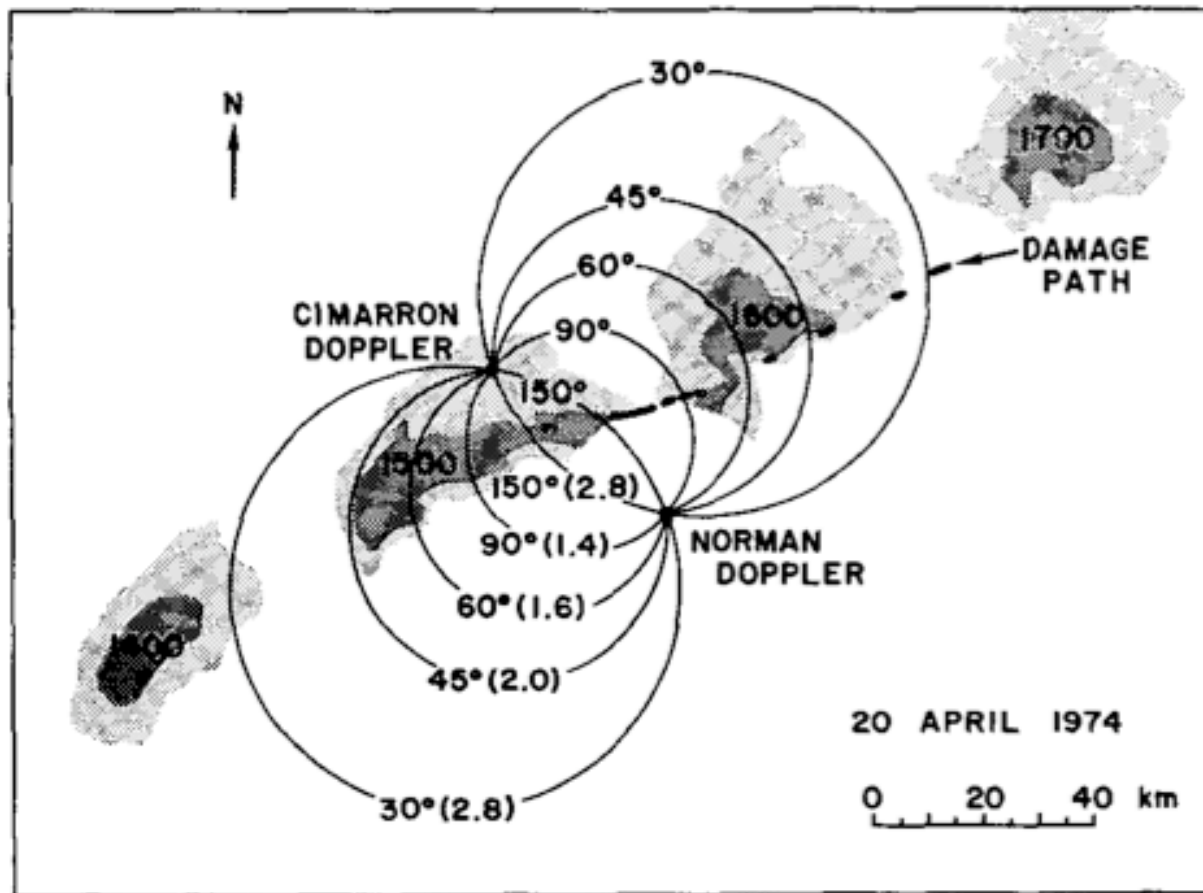
FIG. 1. Nominal dual-Doppler radar coverage area, with labeled circles representing angles between beams from the two radars; value in parentheses are ratios of wind vector RMS error to RMS error in individual Doppler velocity measurements. Hourly echo positions are from the NSSL WSR-57 surveillance radar (echoes within 20 km of radar are masked by ground clutter). Heavy line segments represent tornado damage areas.

Brown et al 1975

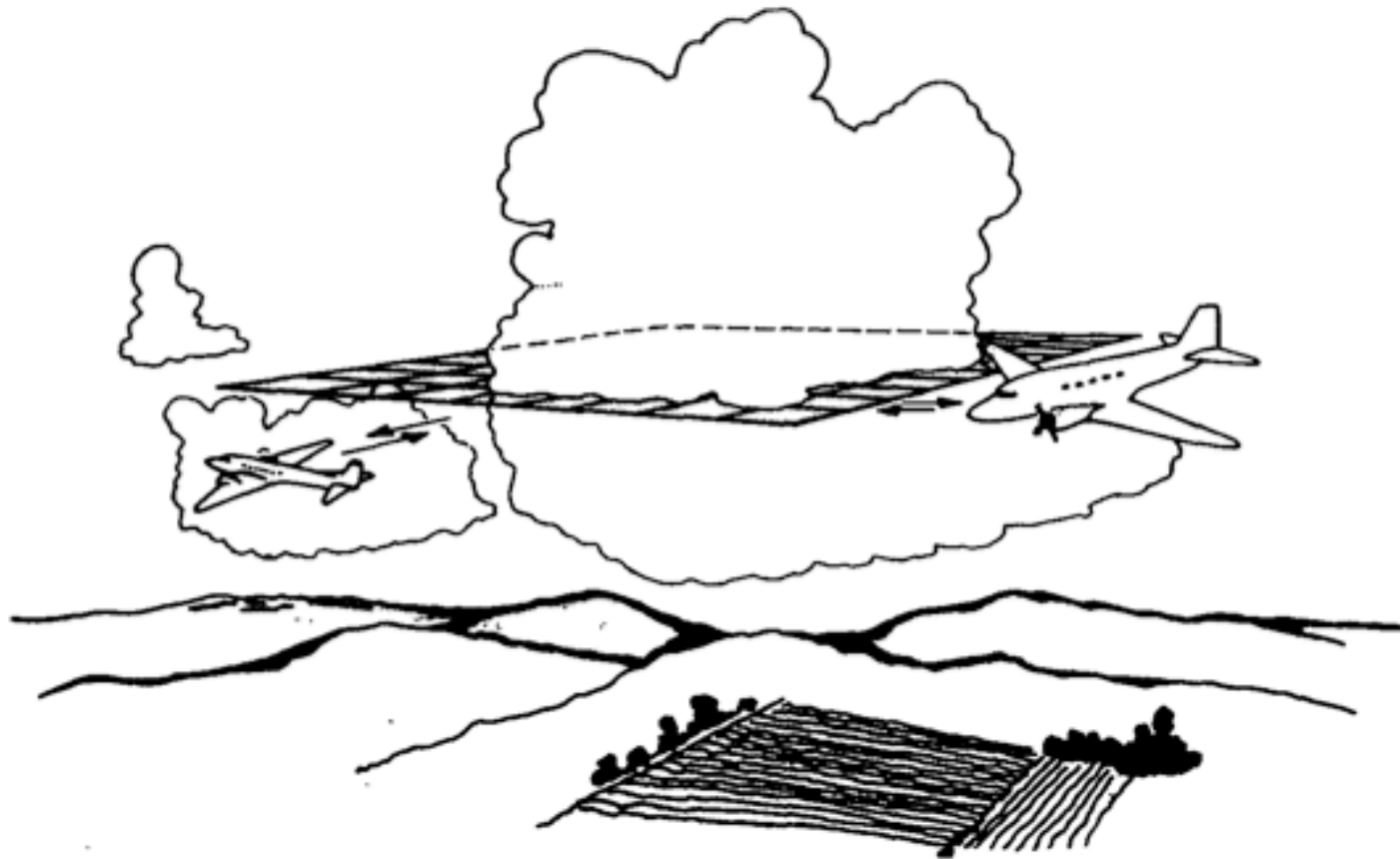6 JUNE 1974   1616 CST   HEIGHT 0.3KM
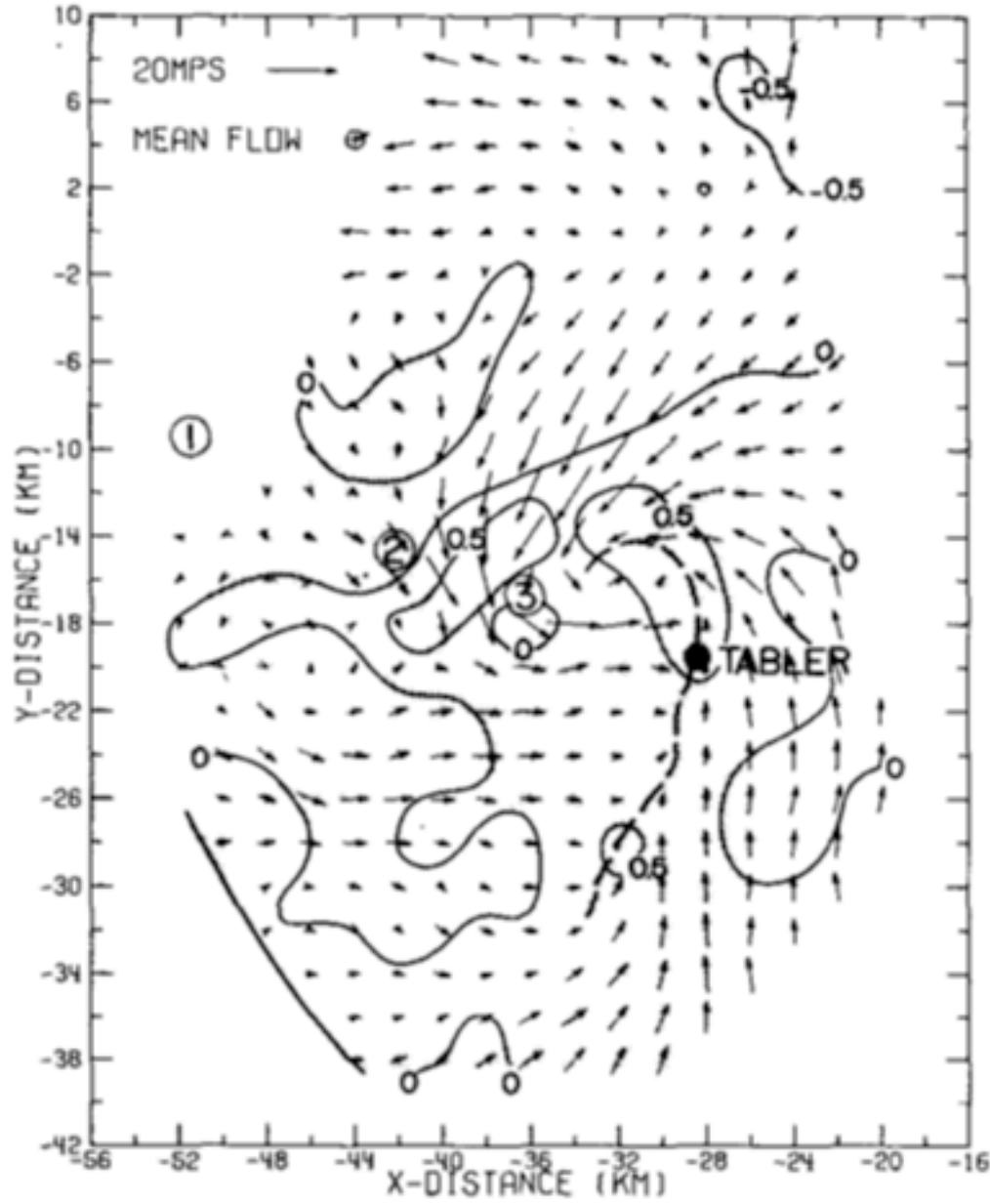
Brandes 1977

FIG. 8. Observing two-dimensional horizontal velocities in a plane defined by the trajectories of two aircraft simultaneously probing the same storm. Only one aircraft is needed if the storm processes are stationary for several minutes.

Lhermitte 1971

FAST
(Fore Aft Scanning Technique)
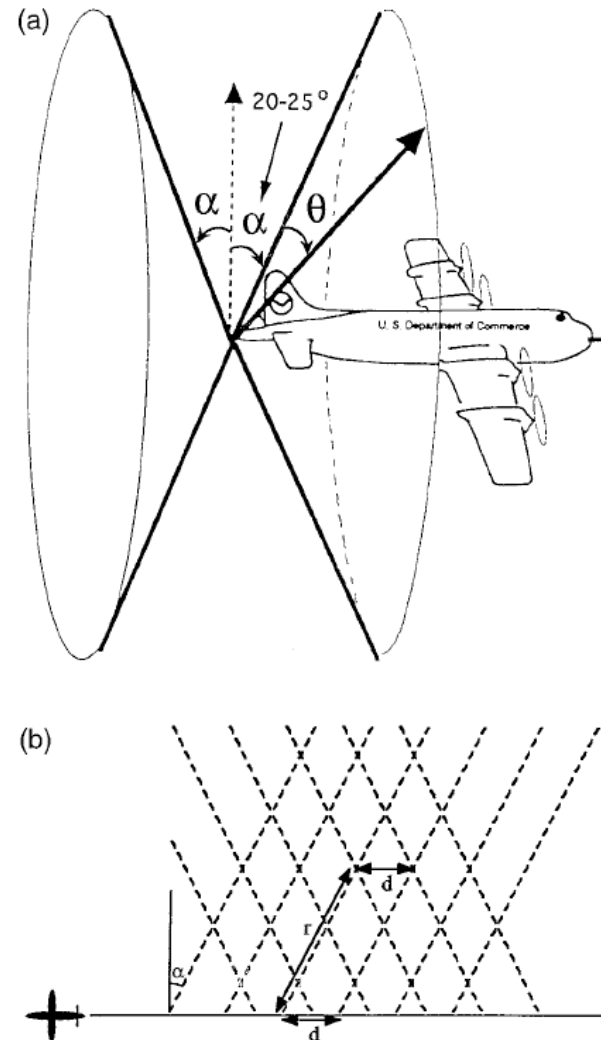
Dowell et al. 1997

FIG. 2. (a) Geometry of the fore–aft scanning technique (adapted from Jorgensen et al. 1995). During a fore scan, $\alpha = +(20°–25°)$ and θ typically advances through the entire interval 0°–360°. (For this study, the values of θ were within only half that interval because the data consisted of "sector scans.") Then during an aft scan, $\alpha = -(20°–25°)$ and θ advances through the desired interval. (b) Radar beam pattern for a single aircraft obtaining pseudo-dual-Doppler data by using the fore–aft scanning technique. Dashed lines indicate fore and aft beams in a horizontal plane at flight level; α, d, and r are the tilt angle of the radar with respect to the flight track (20°–25°), the distance between consecutive fore or aft scans (approximately 1 km), and the range to the target (typically 25 km or less), respectively.

MOBILE DUAL-DOPPLER ANALYSIS

23:40:14 UTC
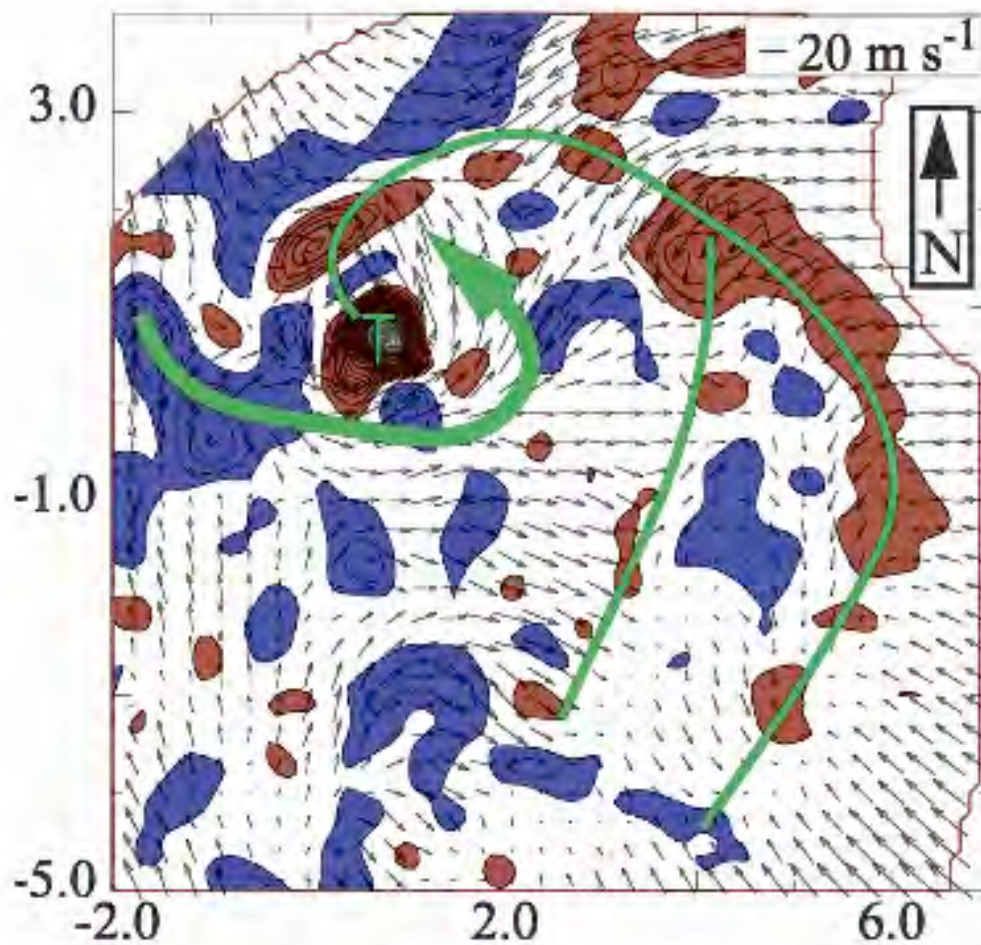
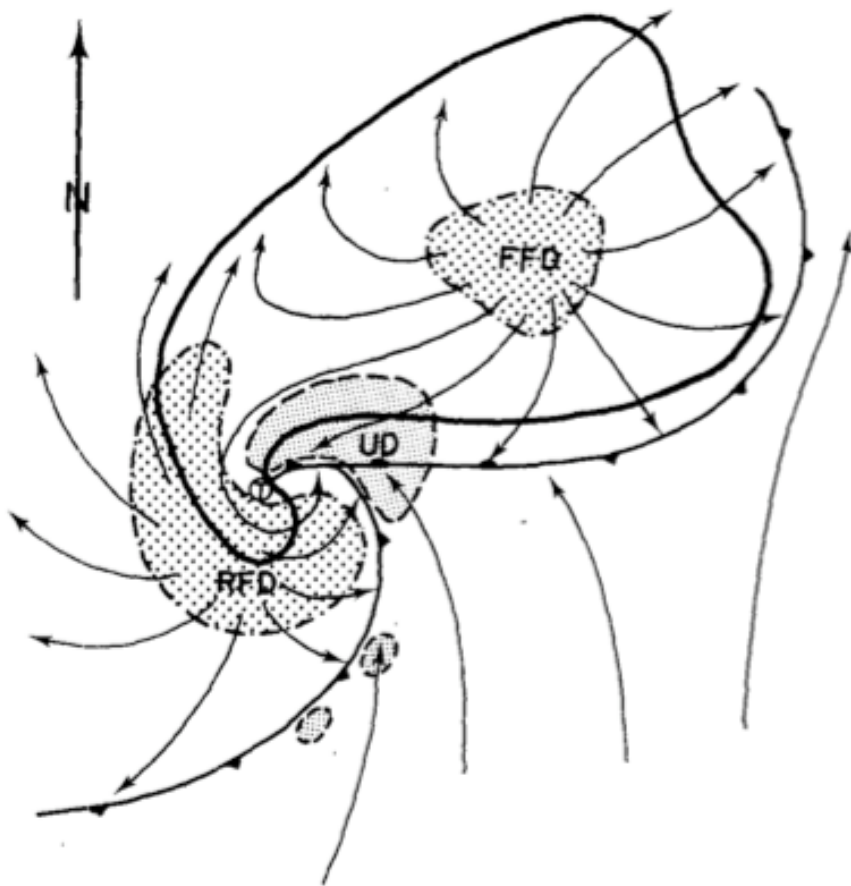Wurman et al. 2007
26 May 1997 Kiefer, OK

FIG. 7. Schematic plan view of a tornadic thunderstorm at the surface. Thick line encompasses radar echo. The thunderstorm "gust front" structure and "occluded" wave are also depicted using a solid line and frontal symbols. Surface positions of the updraft (UD) are finely stippled, forward flank downdraft (FFD) and rear flank downdraft (RFD) are coarsely stippled, along with associated streamlines (relative to the ground) are also shown. Tornado location is shown by an encircled T.

ther, mesonetwork observations also provide evidence of the two distinct downdrafts associated with supercell storms. Surface air beneath the downwind downdraft has a potential wet-bulb temperature (θ_w) that probably results from mixing of updraft (high θ_w) and mid-level environmental (low θ_w) air (Lemon, 1974). This forward flank downdraft forms a relatively weak discontinuity at the surface on the forward and right flanks of the radar echo. As the storm moves, the discontinuity spreads ahead of the echo, but may become quasi-stationary along the right echo flank (Fig. 7).

The existence and strength of the rear flank downdraft is also revealed by the mesonetwork measurements of Charba and Sasaki (1971), Lemon (1976) and Barnes (1978). These observations show θ_w values compatible with mid-level (3–5 km AGL) environmental air, divergence and strong pressure excesses on the storm's rear flank, immediately trailing hook echoes. This air can generally be dis-
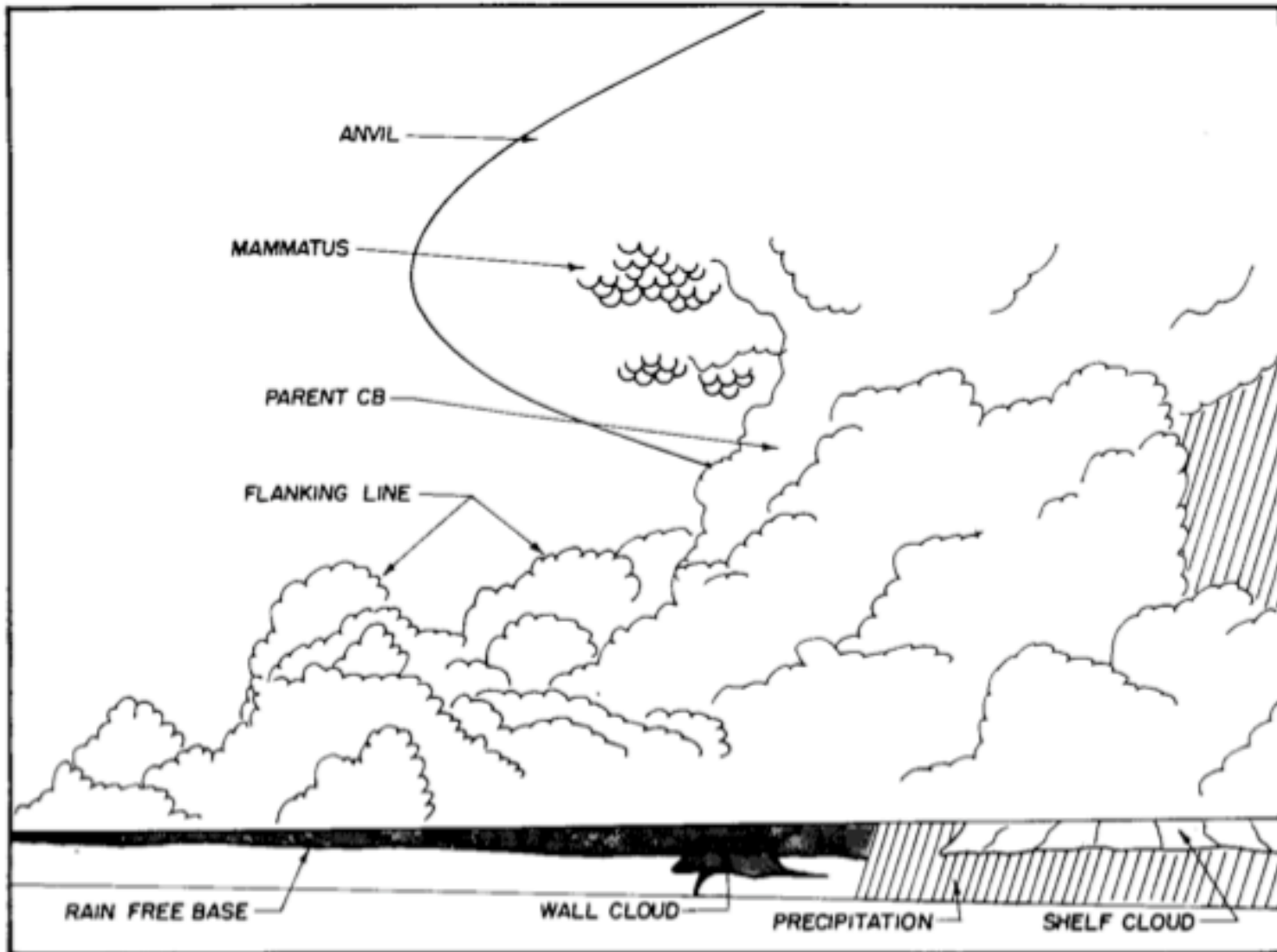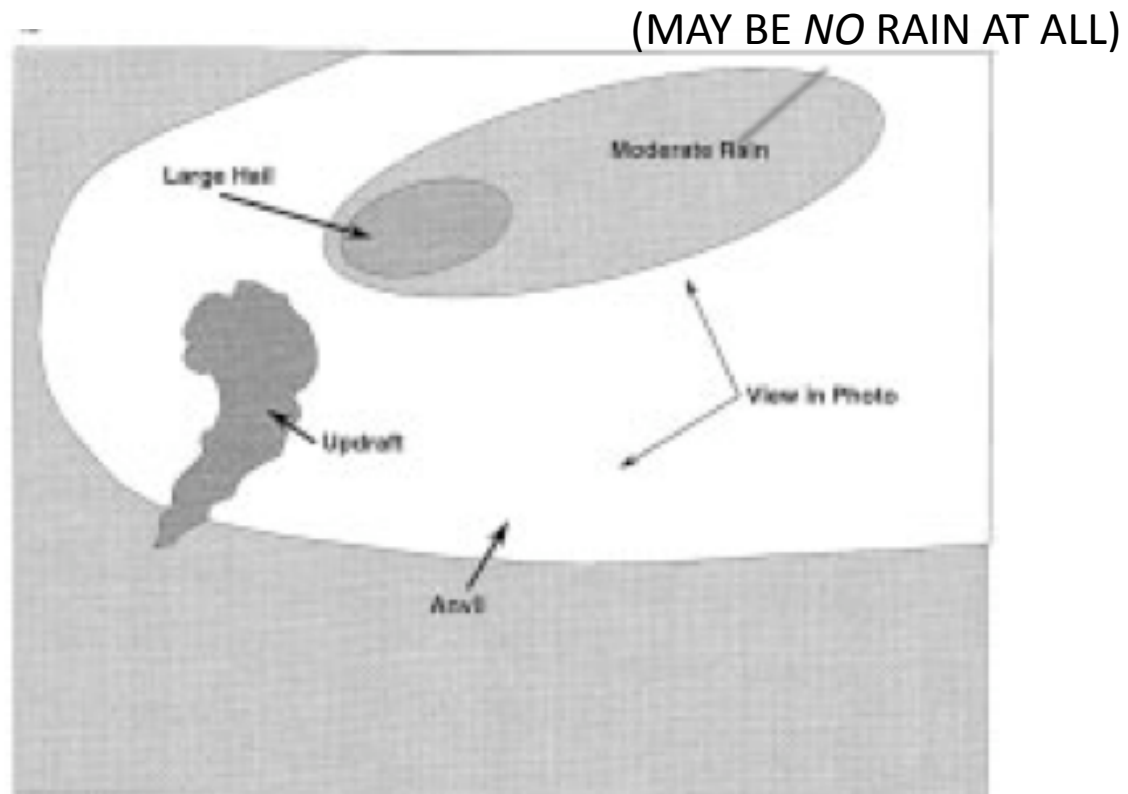
Lemon and Doswell 1979

FIG. 2. Schematic northwestward view (vertical section) of the tornadic thunderstorm shown in Fig. 1.

Moller 1978

Bluestein and Parks 1983
CHARACTER OF PRECIPITATION NEAR UPDRAFT IN SUPERCELLS
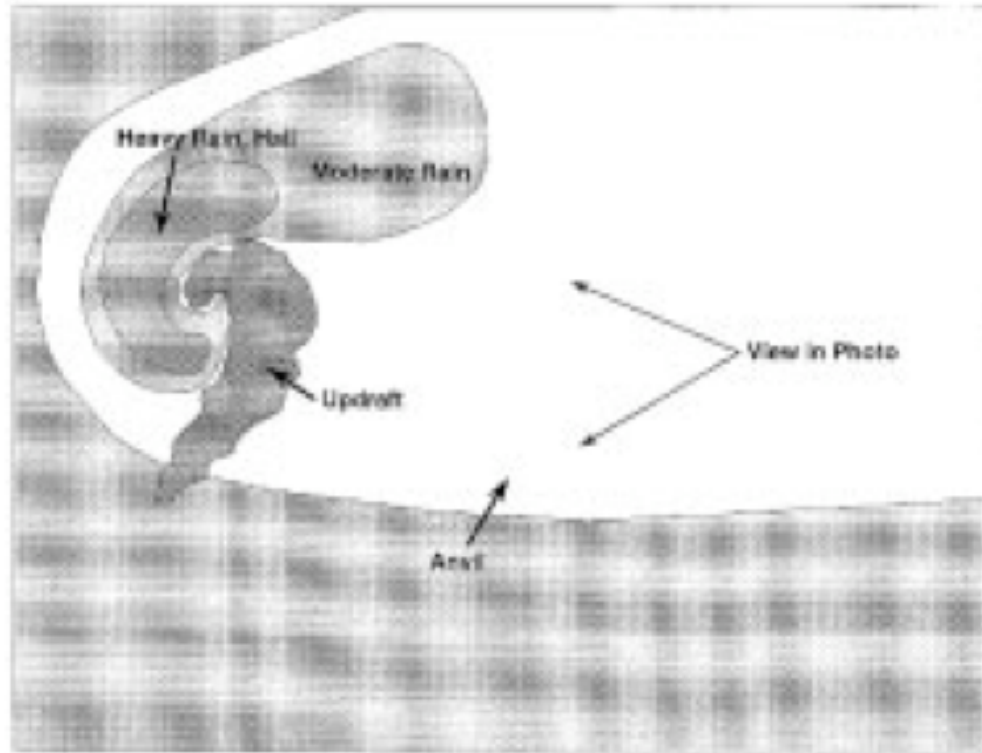
(MAY BE *NO* RAIN AT ALL)
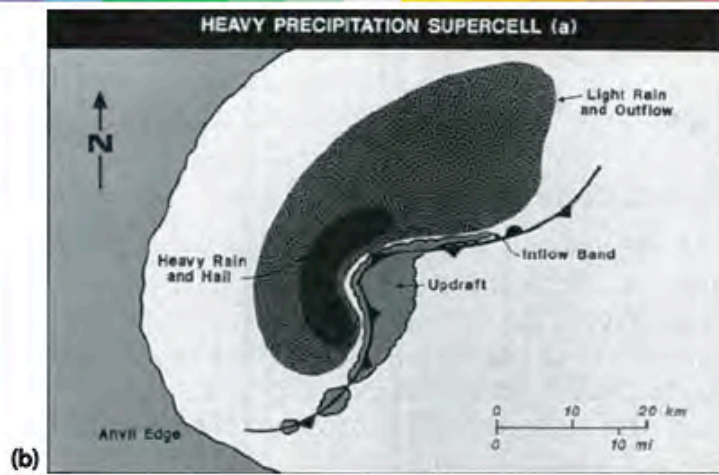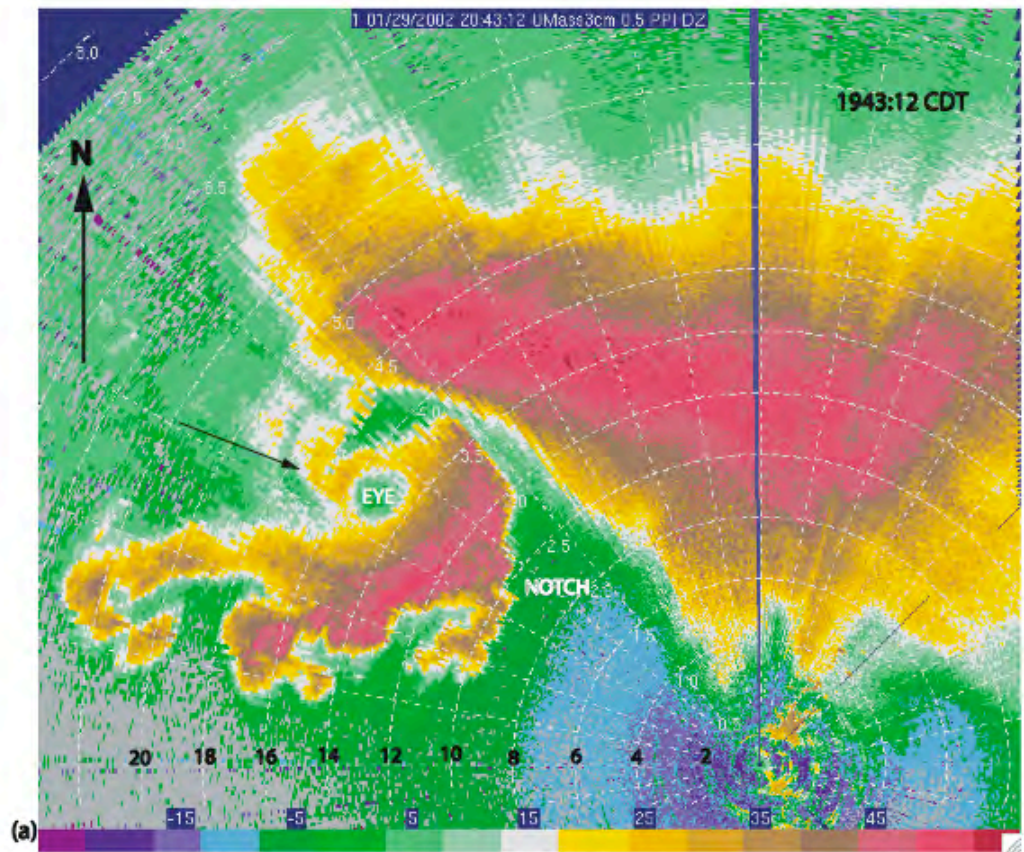

Low-Precipitation (LP) Supercell
Rasmussen and Straka (1998)
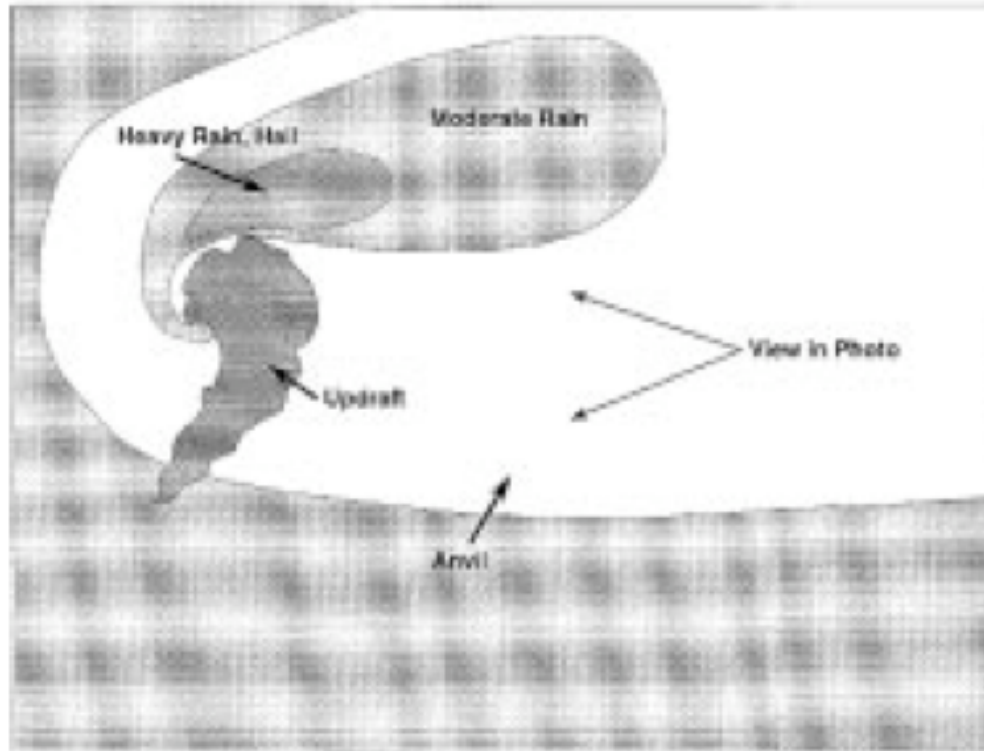
Classic (CL) Supercell
Rasmussen and Straka (1998)

Doswell et al. (1990)

High-Precipitation (HP) Supercell
Rasmussen and Straka (1998)

1 07/29/2002 20:43:12 UMass3cm 0.5 PPI D2

1943:12 CDT

N

EYE

NOTCH

20   18   16   14   12   10   8   6   4   2

-15   -5   5   15   25   35   45

(a)

HEAVY PRECIPITATION SUPERCELL (a)

N

Light Rain
and Outflow

Heavy Rain
and Hail

Inflow Band

Updraft

Anvil Edge

0   10   20 km

0   10 mi

(b)

29 May 2004

Bluestein et al. 2007
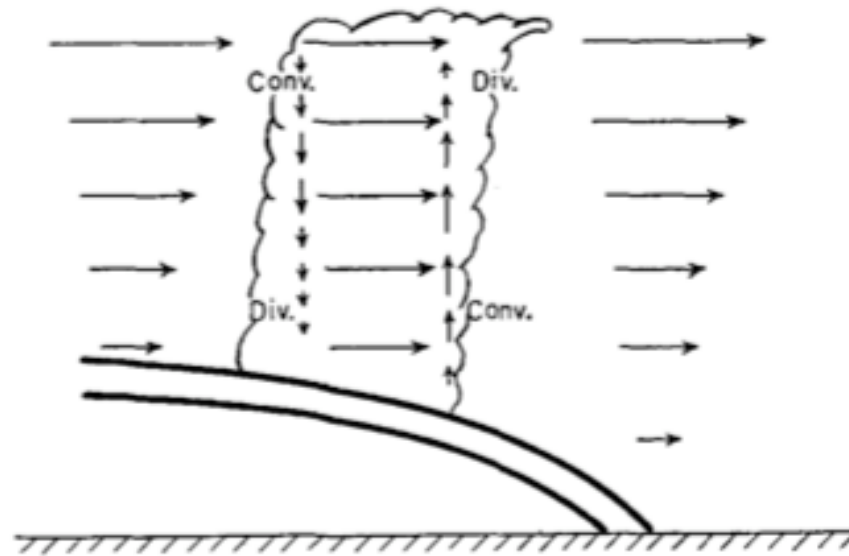
2-D WINDS UNIDIRECTIONAL

FIG. 16. Schematic diagram of cross section through convective cloud region above cold-front surface. Horizontal vectors indicate wind (velocity proportional to length of arrow) at different levels within and outside cloud region. Regions of horizontal divergence and convergence resulting from vertical interchange of horizontal momentum are indicated at cloud boundaries. Vertical vectors indicate consequent vertical acceleration effects.
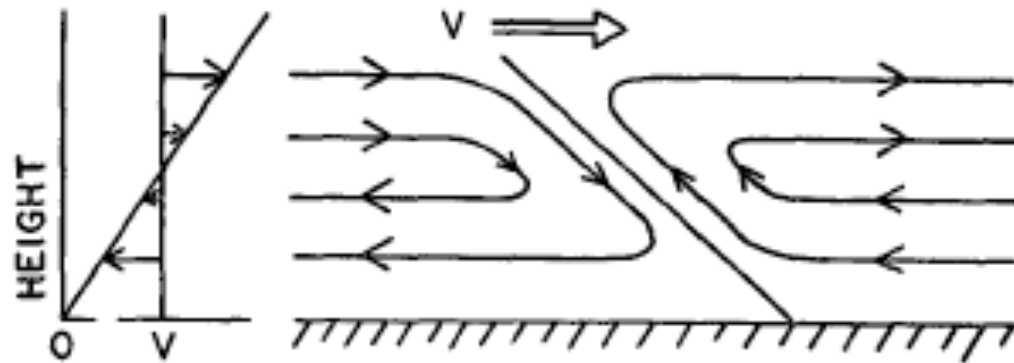
Newton 1950

FIG. 14. Schematic representation of the circulation in a vertical section through a convective disturbance along its direction of travel (from left to right), when the direction of the winds in its environment is constant with height and the variation of wind-speed relative to the disturbance is as shown on the left (after Browning and Ludlam, 1962).
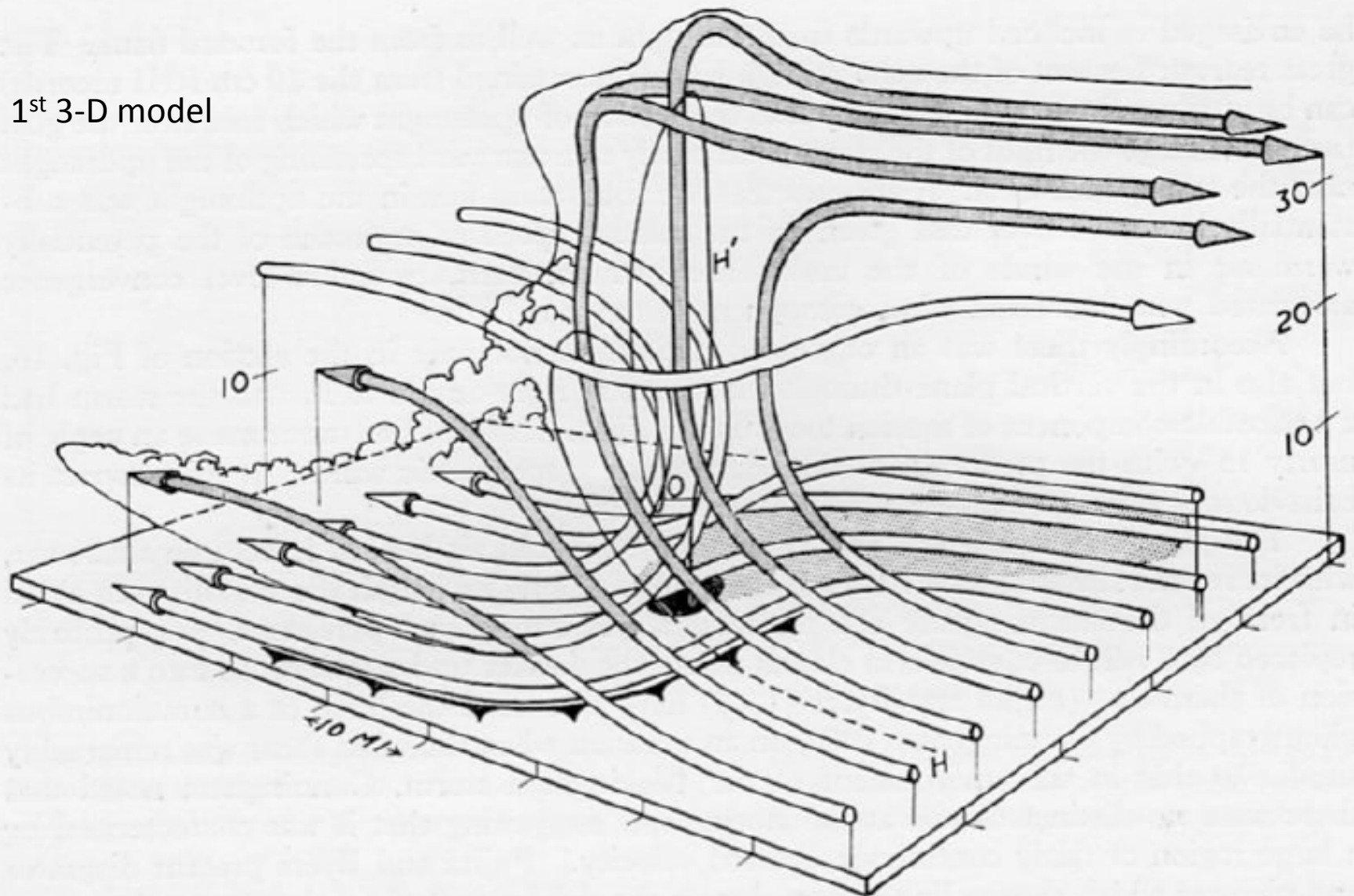
2-D WINDS UNIDIRECTIONAL

1st 3-D model

Figure 17. Three-dimensional model of the airflow within the Wokingham storm. Streamlines of air in which condensation has occurred are shaded.

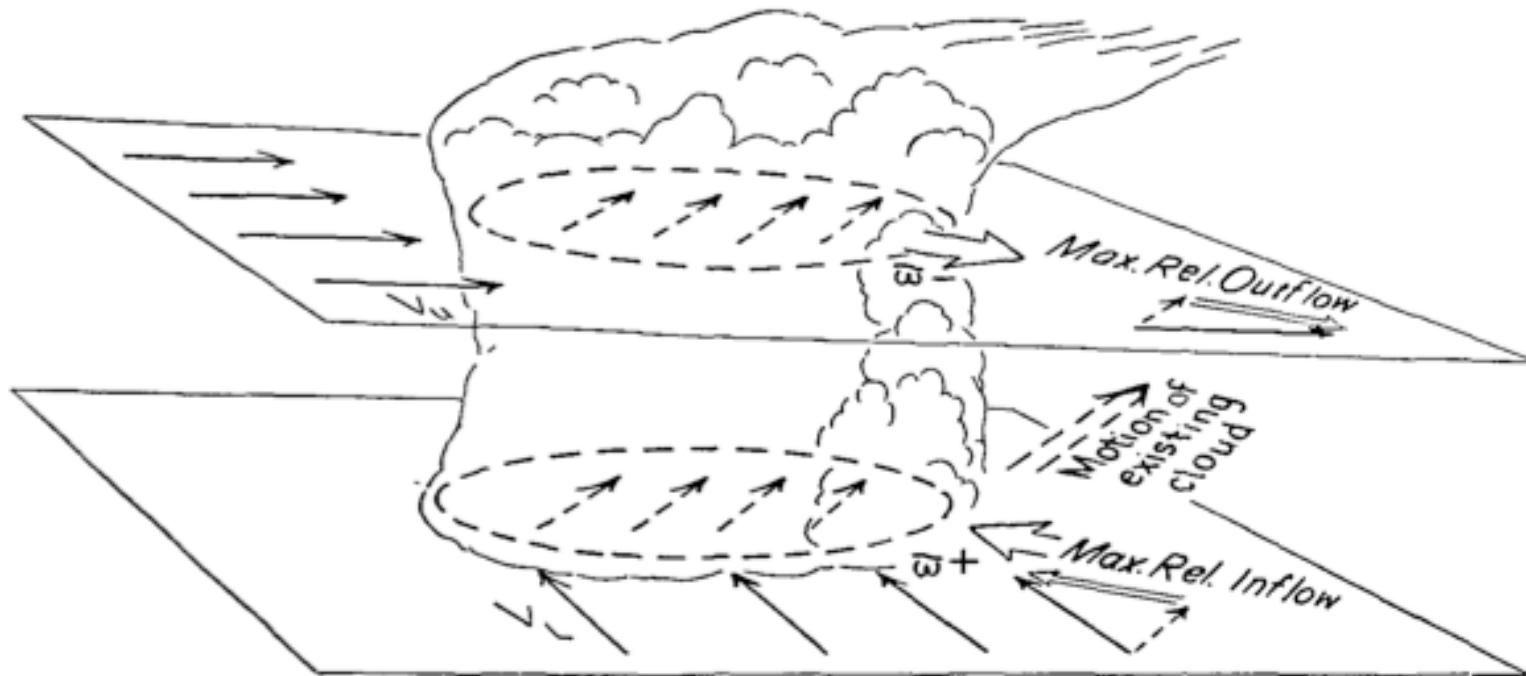Browning and Ludlam 1962

WINDS NOT UNIDIRECTIONAL

FIG. 6. Sketch of convective storm in environment wherein wind veers with height.
See text (after Newton, 1960).
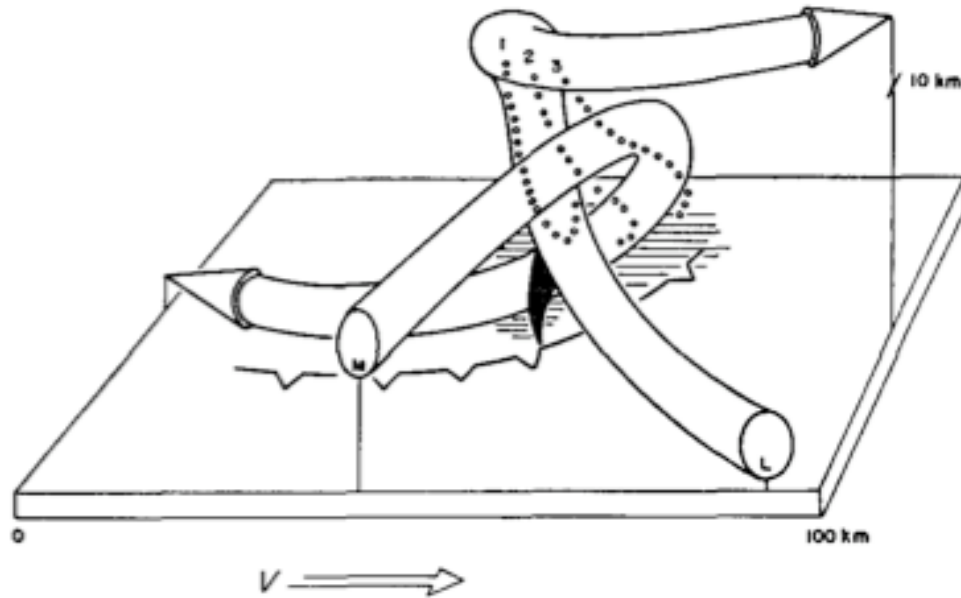
Newton and Fankhauser 1964

FIG. 2. *Three-dimensional model of the airflow within an SR storm* (i.e., a severe storm which travels to the right of the winds in the middle troposphere). Updraft and downdraft circulations are depicted *relative to the storm itself*, being represented schematically without regard to convergence. L (low) and M (middle) refer to the predominant levels of origin of the updraft and downdraft, respectively. Also shown are some precipitation trajectories (cf. Fig. 5), the approximate extent of precipitation at the surface (hatched area), and the positions of the surface gust front and the tornado (when present). Finally, note the five-fold exaggeration of the vertical scale.
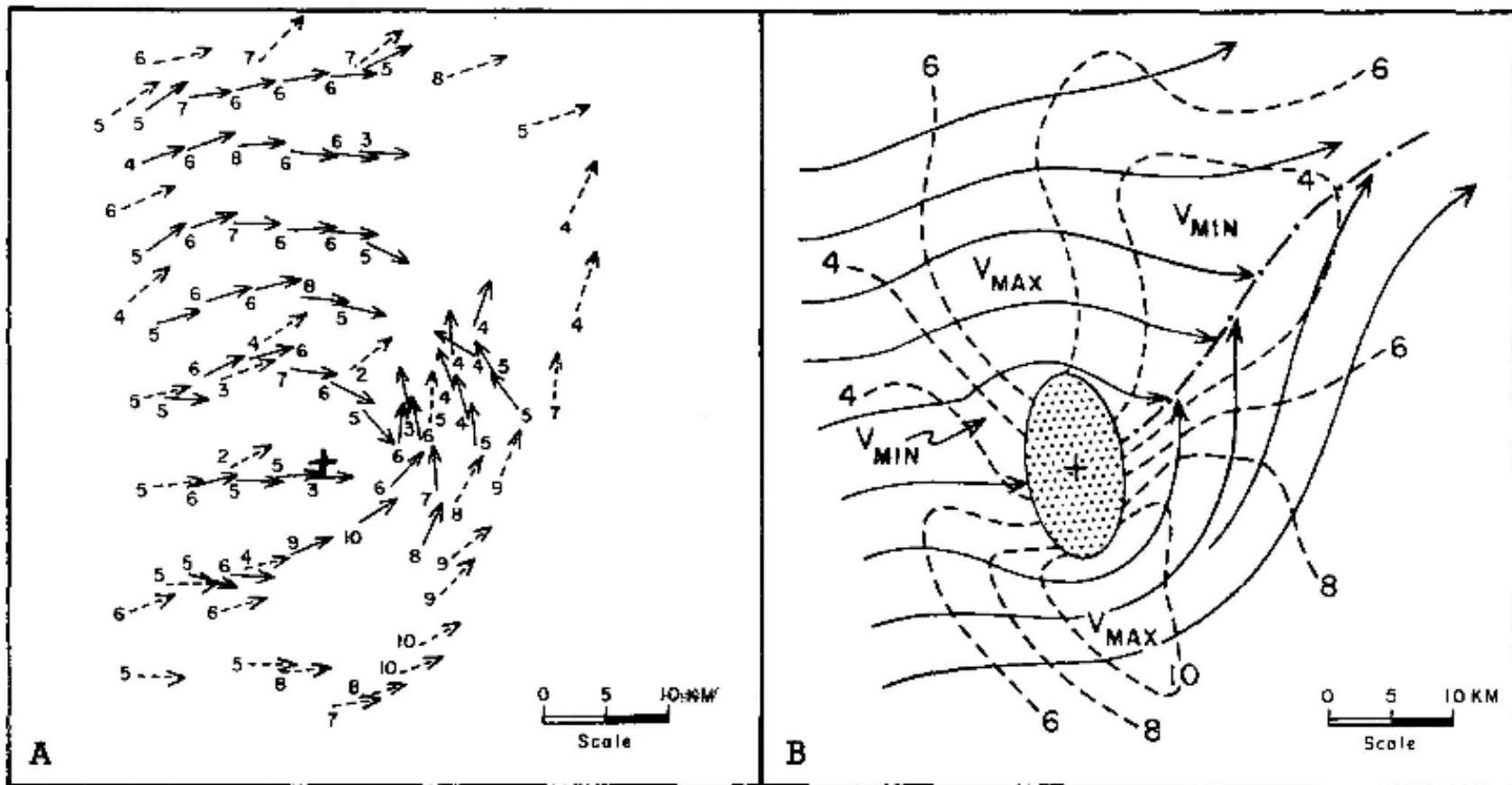
Browning 1964

FIGURE 16.—(A) composite 500-mb relative wind field around the thunderstorm centered on the cross, derived from aircraft measurements (dashed) and chaff displacement (solid). The vector magnitude (m s⁻¹) appears at the tail. (B) synthesized streamline and isotach pattern based on winds in (A). The dash-dot line denotes the wake axis.

Fankhauser 1971
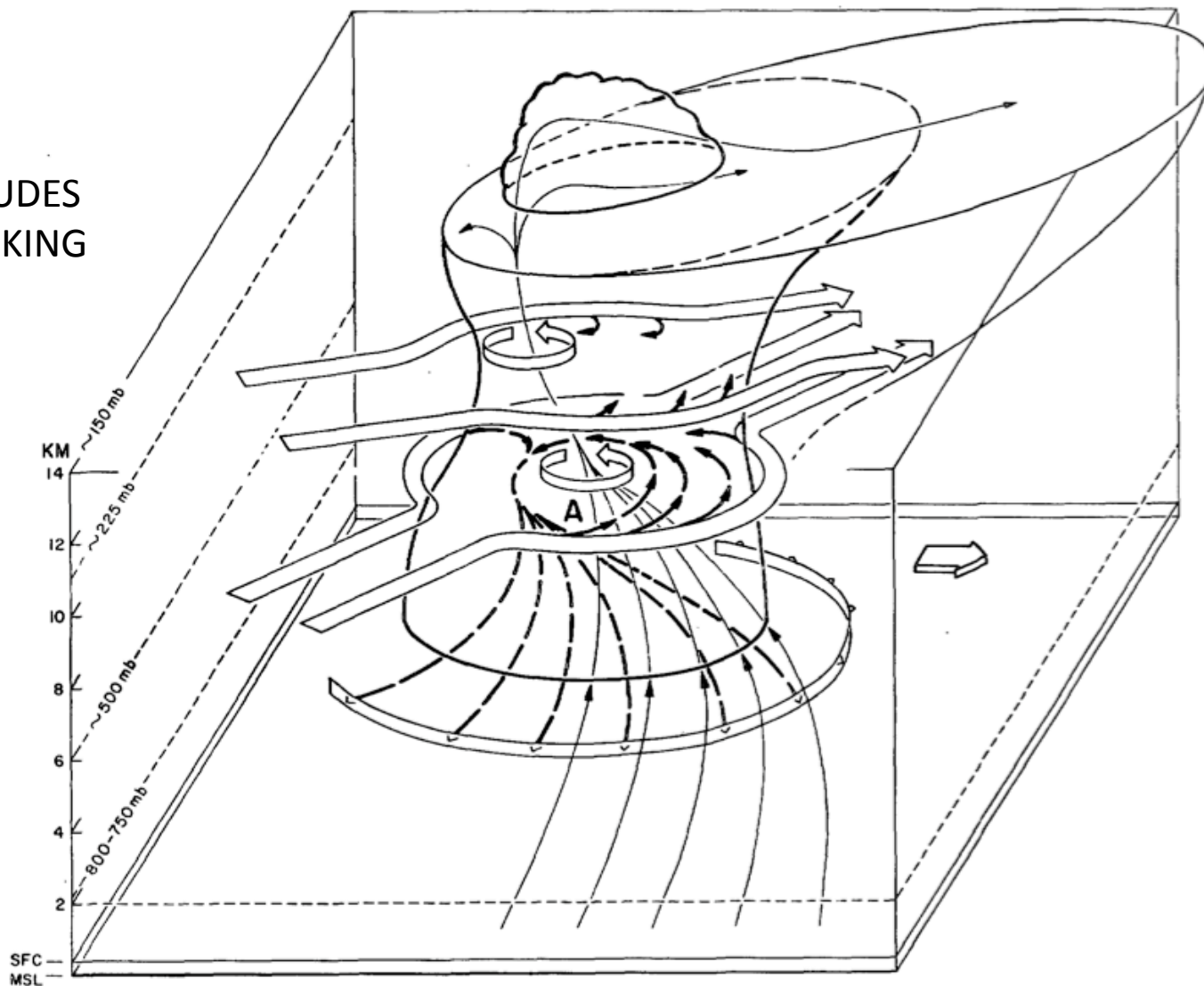
3-D
INCLUDES
BLOCKING

KM

FIGURE 19.—Three-dimensional interpretation of the interacting external and internal air flow associated with an individual persistent Great Plains cumulonimbus, accommodating the impressions from earlier works and features observed in two Oklahoma field experiments. The thin, solid inflowing and ascending streamlines represent the history of moist air originating in the subcloud layer (surface to ~ 750 mb). The heavy dashed streamlines trace the entry and descent of potentially cold and dry middle-level (700- to 400-mb) air feeding downrushing and diverging downdraft. The surface boundary between the inflow and downdraft is shown as a barbed band. The internal circular bands signify net updraft rotation. The shape and orientation of the dividing external bands represent typical vertical shear and character of ambient relative horizontal air flow at middle (~ 500-mb) and upper (~ 225-mb) levels. The approximate pressure-height relationship is shown on the left forward corner of the perspective box. The broad flat arrow on the right represents direction of travel.
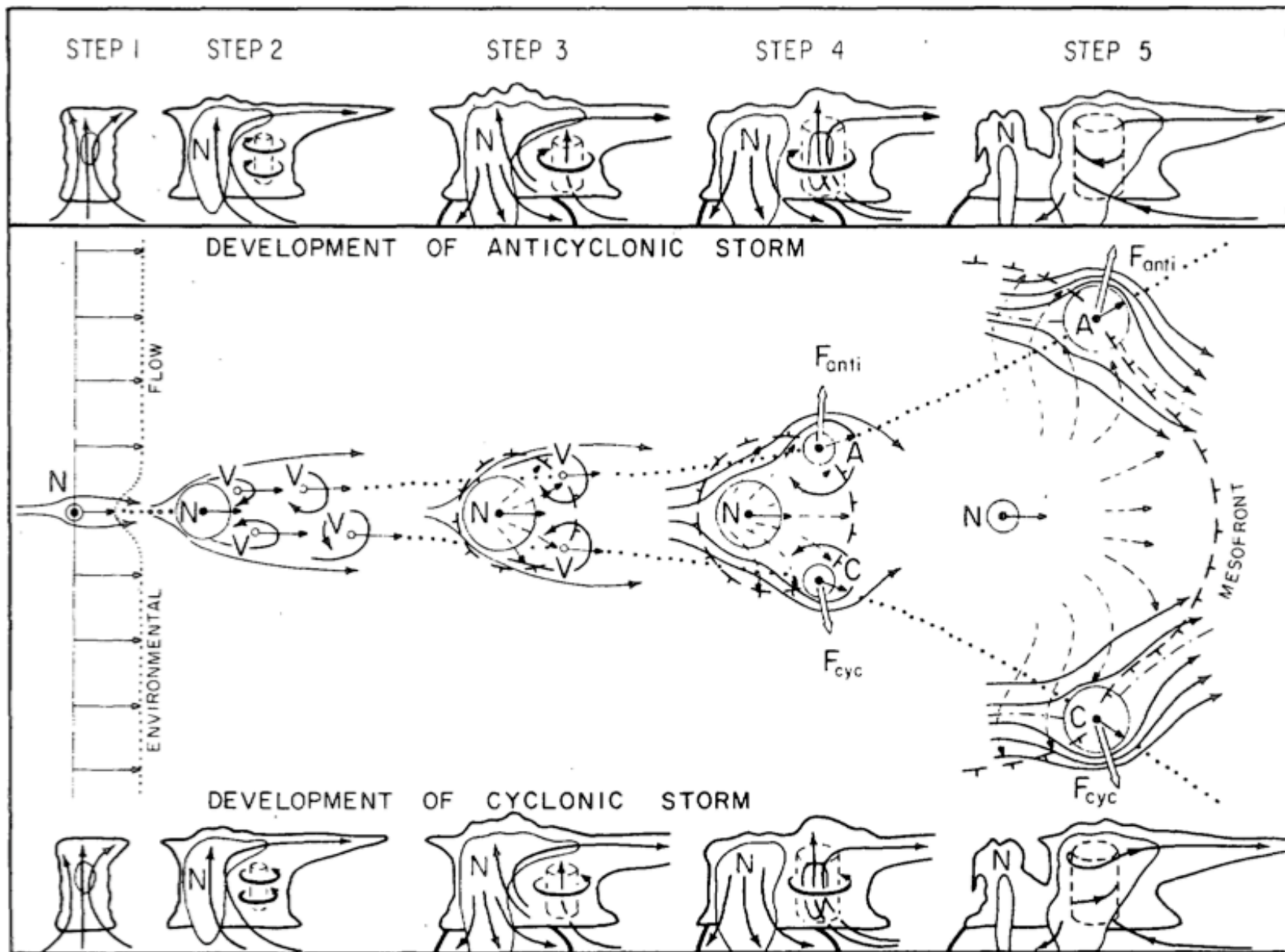
Fankhauser 1971

FIGURE 22.—Schematic diagram showing sequential development of diverging echo couplets. The N designates the initial thunderstorm echo; the A and C refer to the left- and right-moving members formed in anticyclonic and cyclonic shear zones, respectively (after Fujita and Grandoso 1968).

NONLINEAR TERMS
UNI-DIRECTIONAL SHEAR

(a)
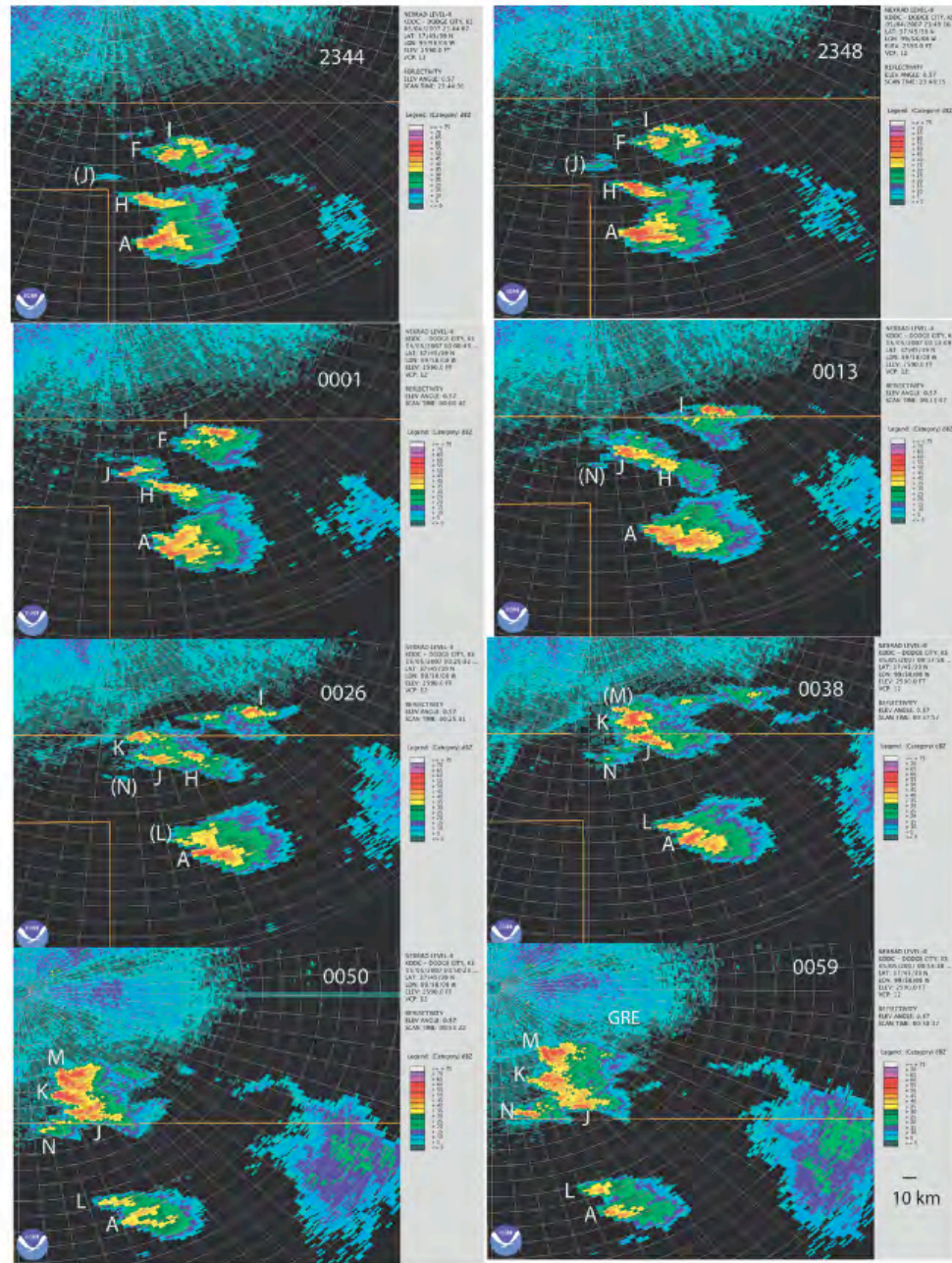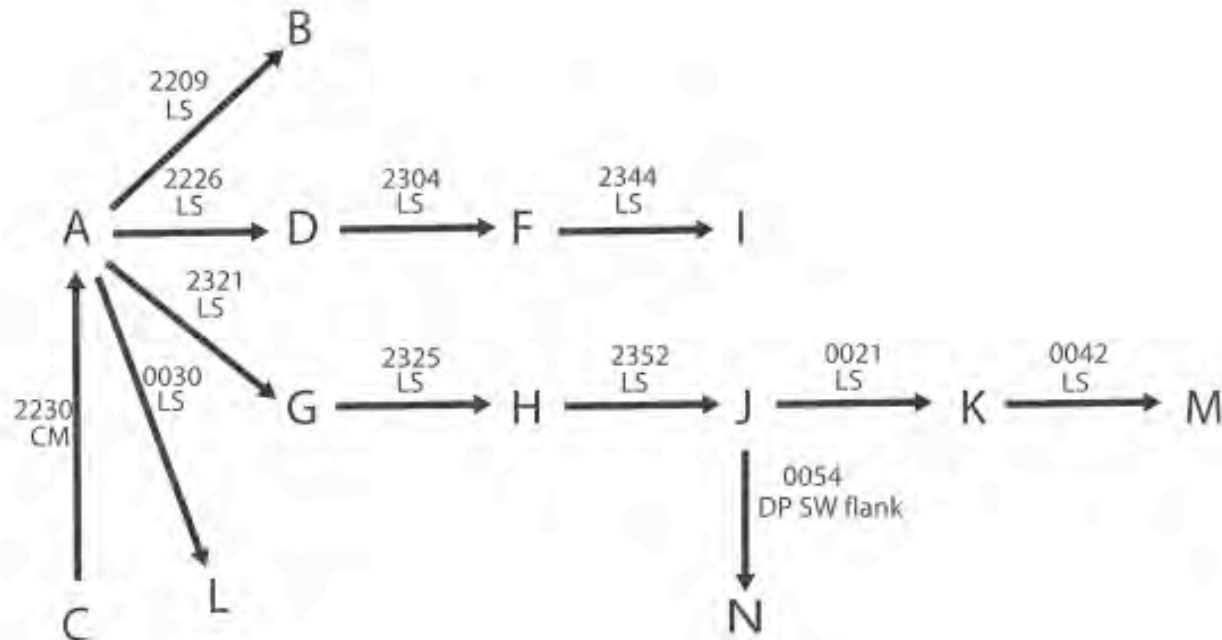
Klemp 1987

SPLITTING

(b)
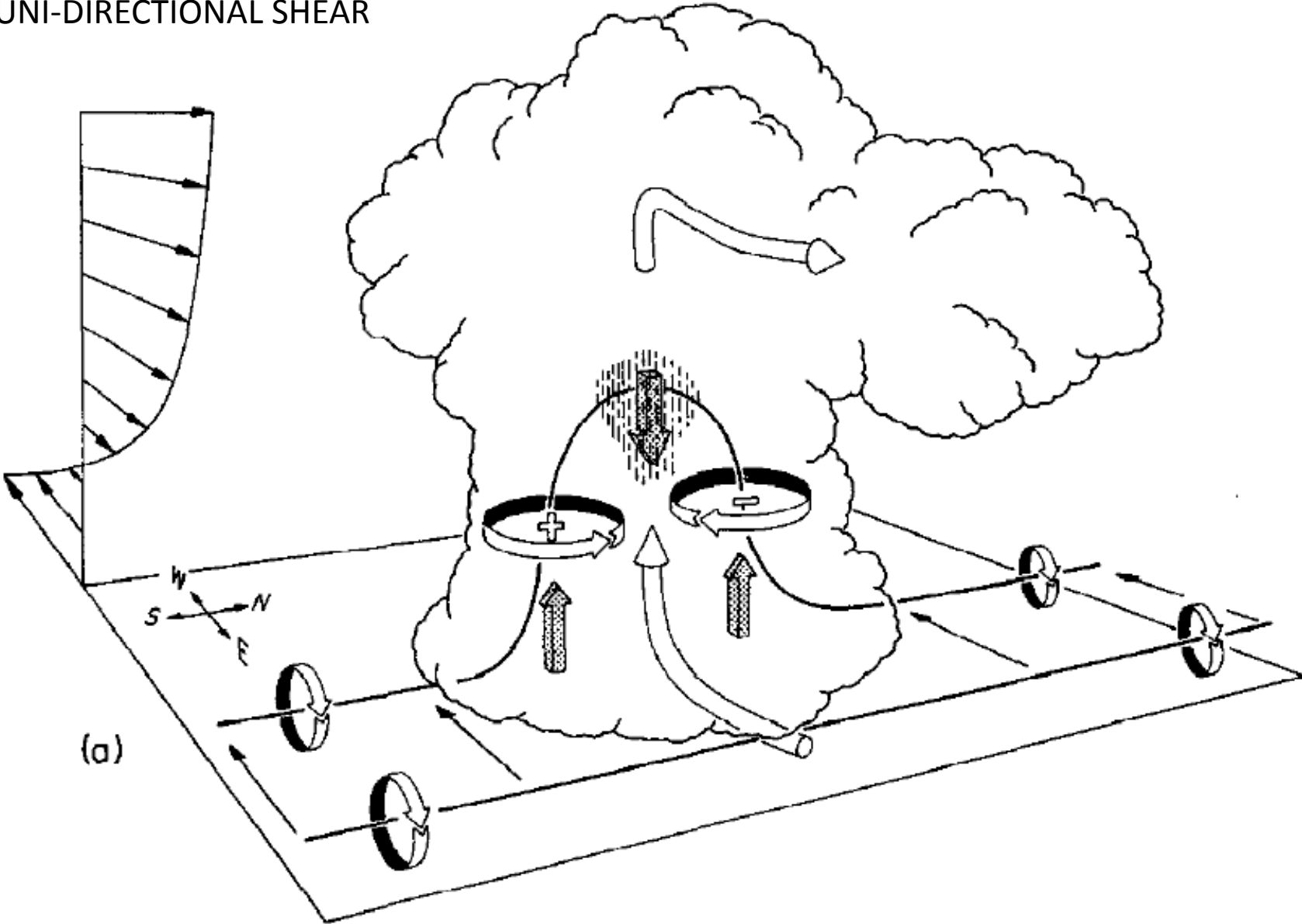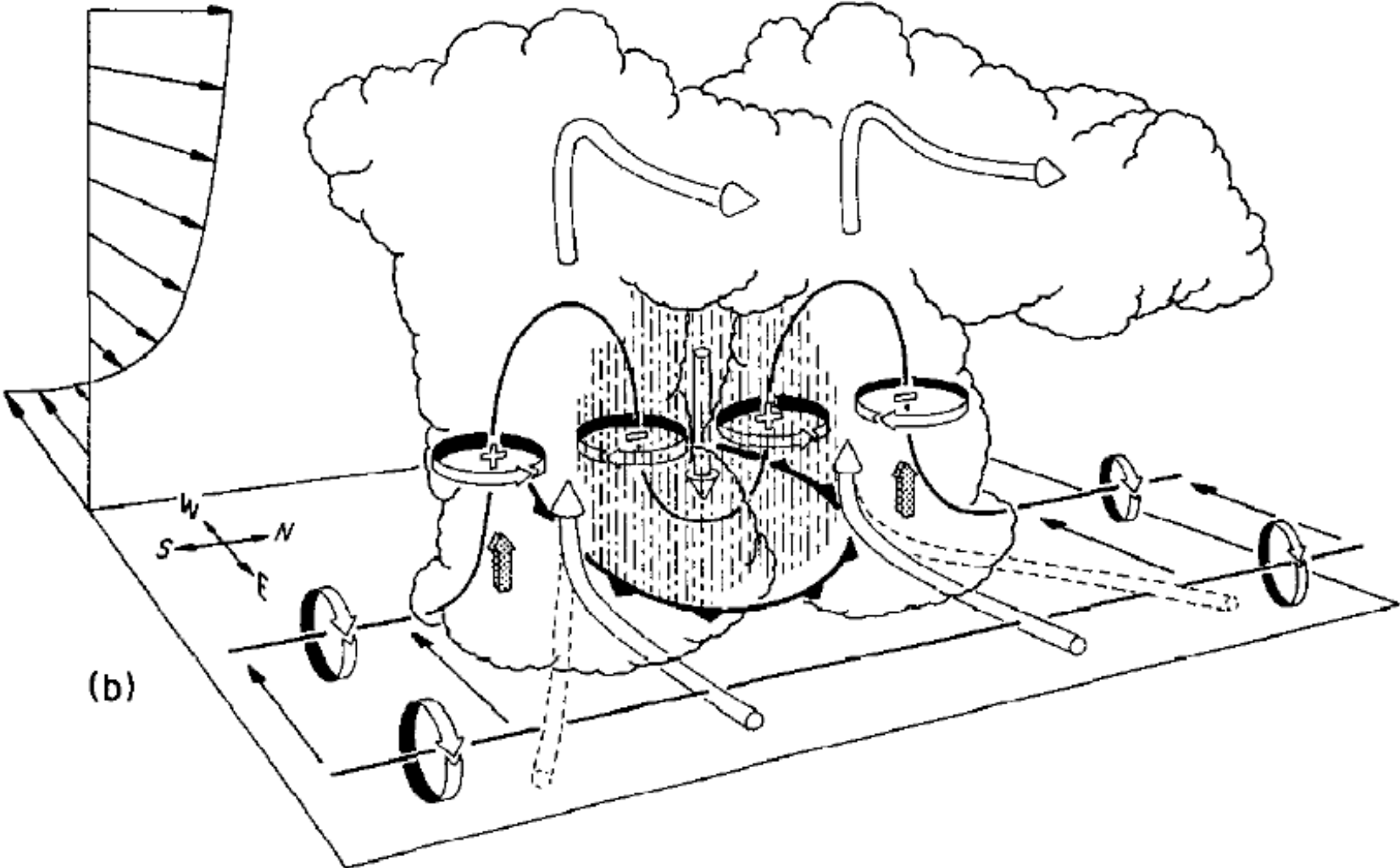
Klemp 1987

FIG. 8. As in Fig. 7 but with a more detailed depiction of the evolution of storm N, at shorter time intervals, from J, a left-split cell from H, from 2344 to 0059 UTC 4/5 May 2007. Reflectivity color scale as in Fig. 7. From the DDC WSR-88D only.

Bluestein 2009

CELL GENEALOGY

FIG. 9. Schematic of the cell genealogy on 4/5 May 2007. Storm names are explained in the text: LS, left split; CM, cell merger; and DP, discrete propagation. The times (UTC) of the left splits, cell merger, and discrete propagation are noted.
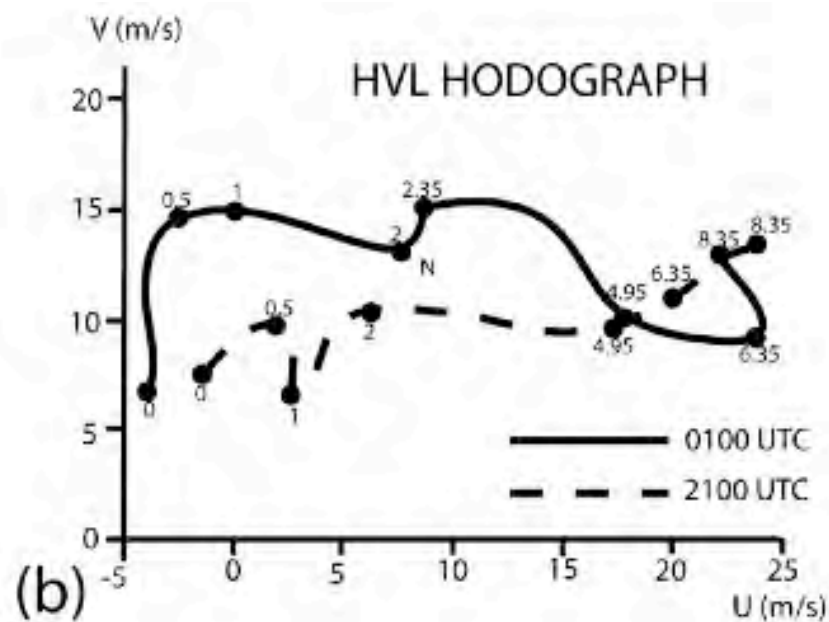
Bluestein 2009

FIG. 4. (a) Time–height cross section of wind data (plotted as in Fig. 1) from the HVL NOAA wind profiler from 2100 UTC 4 May 2007 until 0200 UTC 5 May 2007, up to 7.5 km MSL (up to 6 km AGL). (b) Hodograph for HVL (see Fig. 6). In (b), winds are plotted in km AGL for 2100 UTC (just before storms formed) and 0100 UTC (while storms were on going and storm evolution was occurring, about 1 h before the birth of the Greensburg tornado) on 4/5 May 2007. Motion of storm N, the Greensburg storm (see Fig. 6), is indicated by "N."
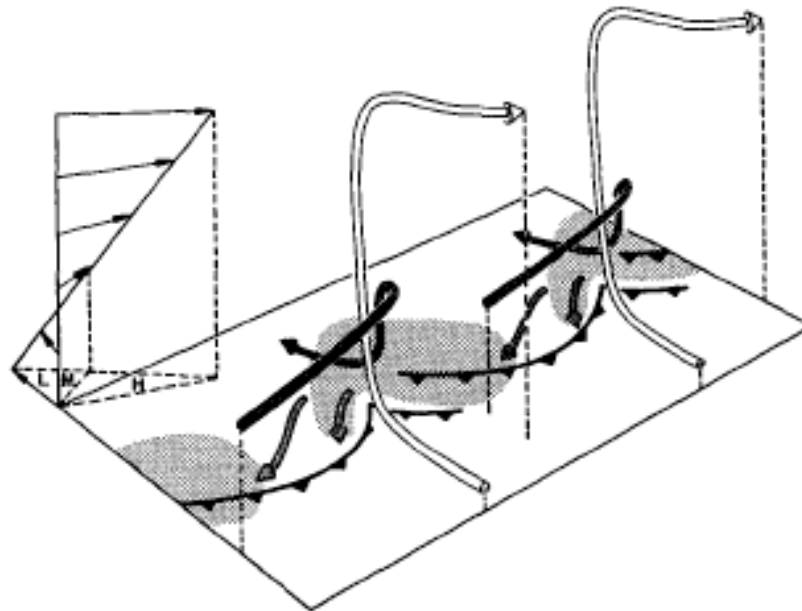
Bluestein 2009

FIG. 4. Lilly's proposal for a line of supercell thunderstorms existing at an angle to the shear so that each supercell could propagate without colliding with a neighbor. The shear profile is indicated on the left; the relative winds at low, middle and high levels are indicated by the L, M and H symbols, respectively. The stippled region indicates the 'hook-shaped' rain area at the surface and the barbed line represents the micro-cold front. (Adapted from Fig. 14 of Lilly, 1979.)

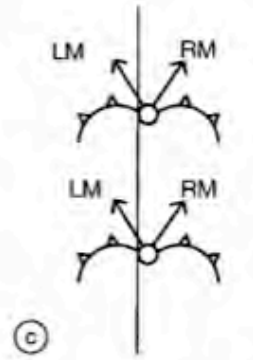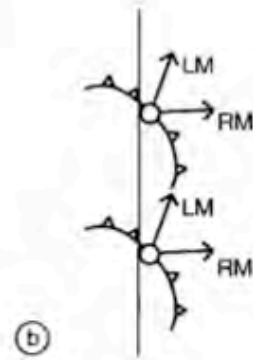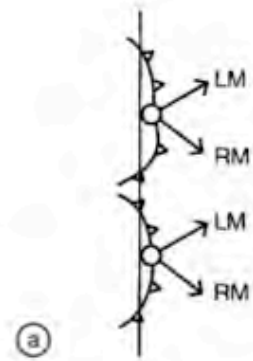Rotunno et al. 1988
(from Lilly 1979)

FIG. 2. Idealized illustration of the relationship between the orientation of the line of forcing (initial thermal bubbles indicated by circles along a vertical line) and the vertical-shear vector (at right). Outflow boundaries denoted by cold front symbol; RM and LM denote storm motion (vectors) of subsequent right- and left-moving cells.
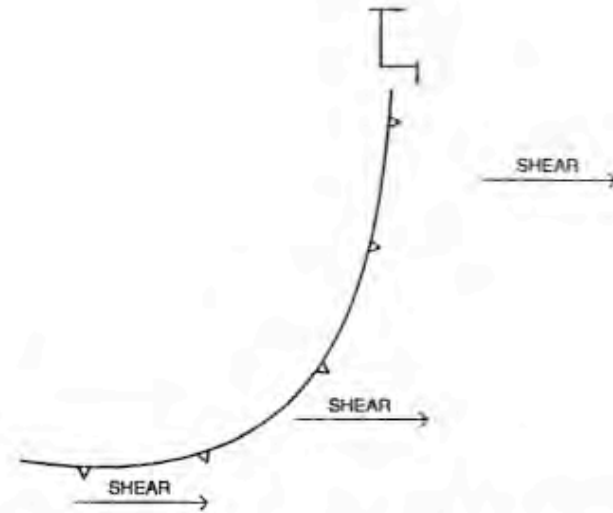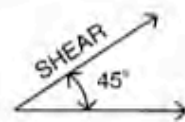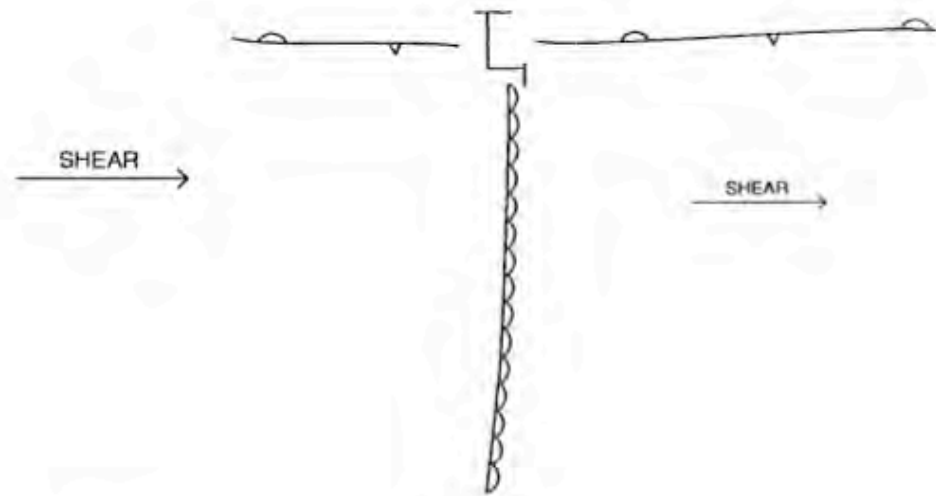
FIG. 3. Typical synoptic features at the surface in the plains region of the United States. (a) Dryline–front intersection, with low pressure area (cyclone). (b) Cold front and low pressure area (cyclone). Vectors represent vertical shear; L denotes low pressure area associated with the cyclone. Dryline in (a) is represented by a scalloped line.

Bluestein and Weisman 2000

(a) 20 KM α = 90°

(b) 20 KM α = 45°

(c) 20 KM α = 0°

(d) 20 KM α = 135°

Bluestein and Weisman 2000

LINEAR TERMS
UNI-DIRECTIONAL SHEAR

(a)

Klemp 1987
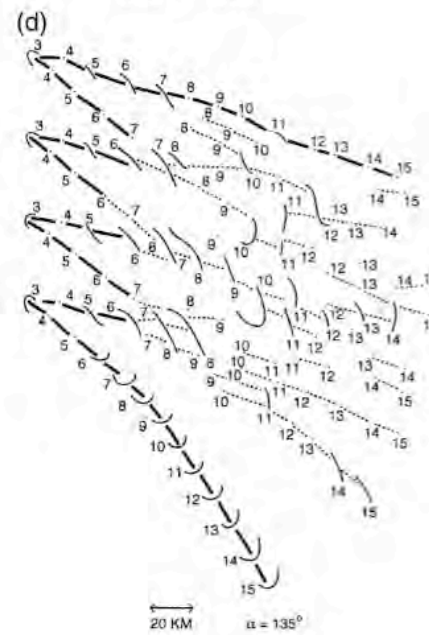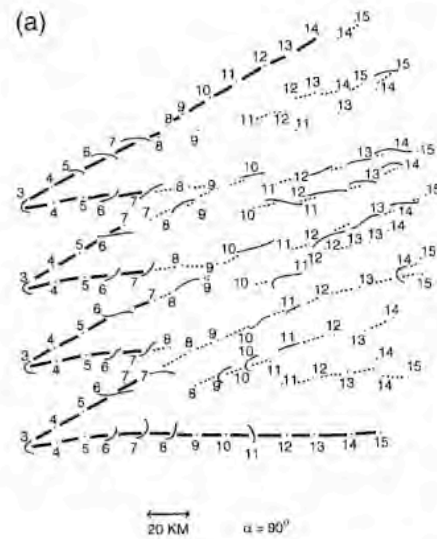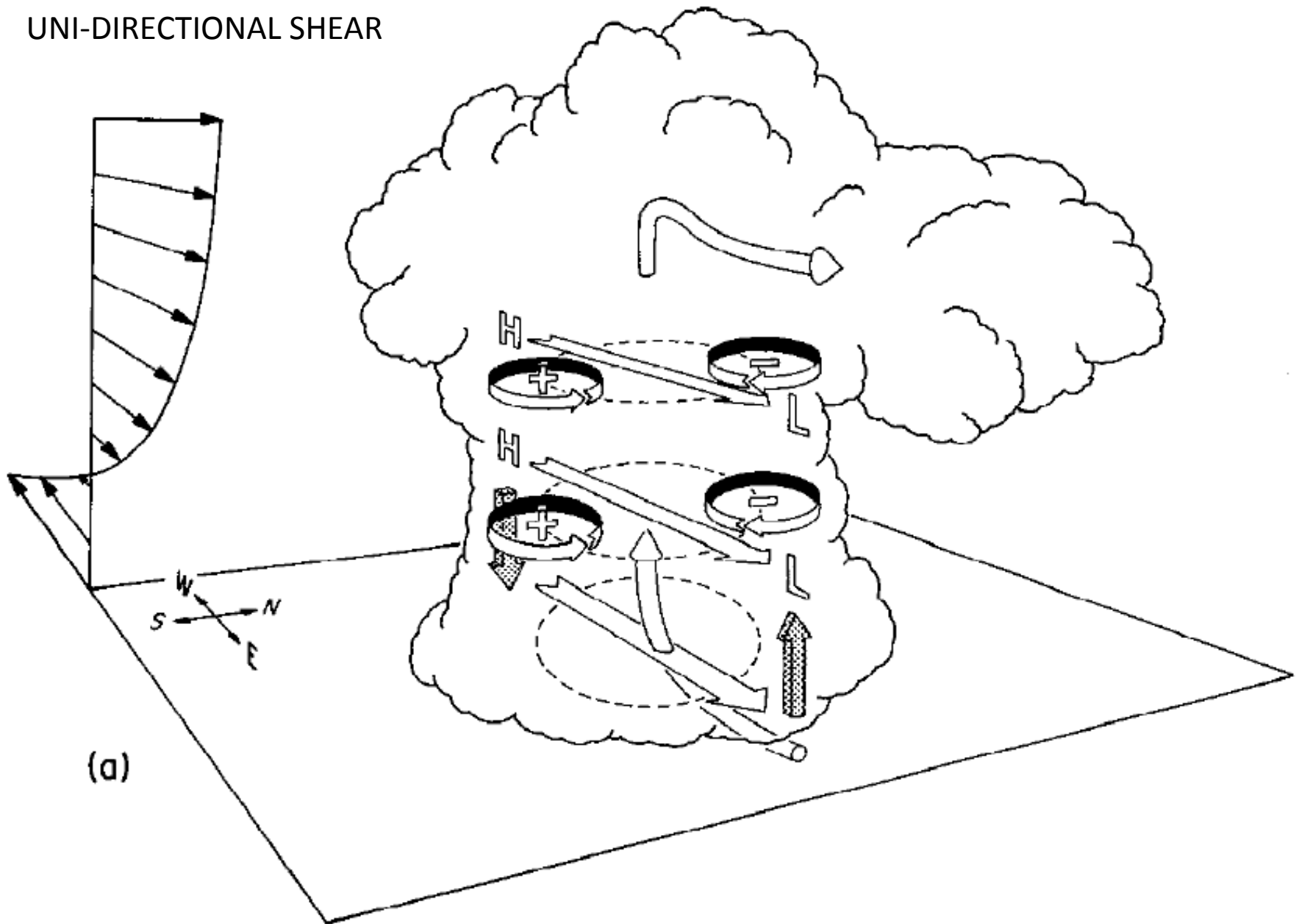
LINEAR TERMS
DIRECTIONAL SHEAR

(b)

Klemp 1987
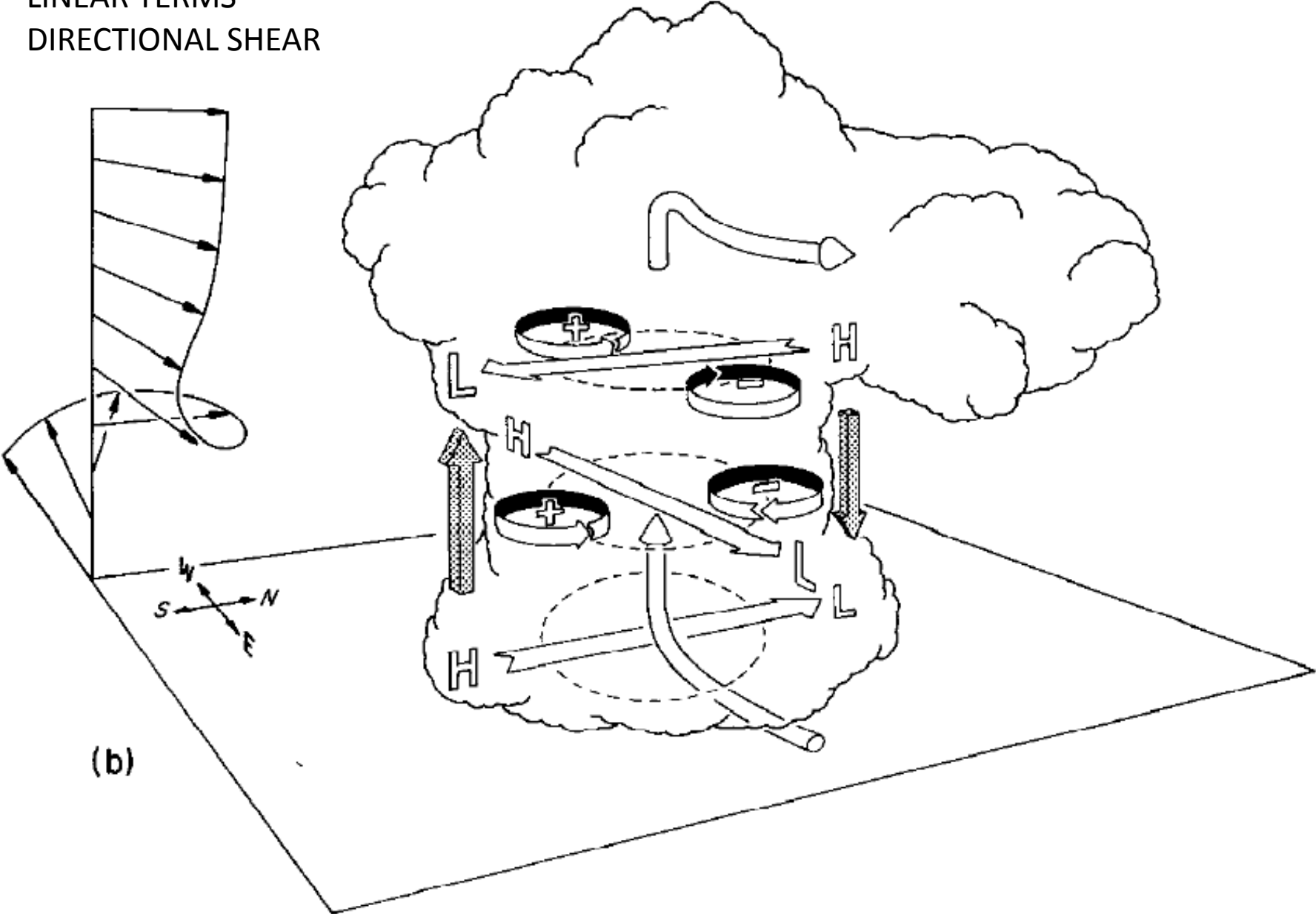
HELICITY DISCUSSION
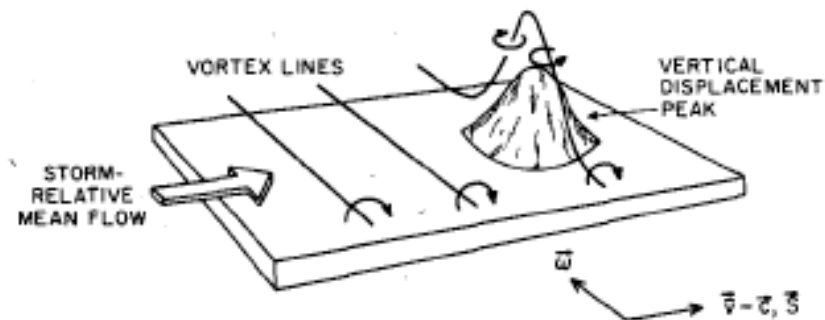
FIG. 7. Effect of localized vertical displacement "peak" (i.e., "hump" in isentropic surface) on vortex lines when mean vorticity ω and mean storm-relative flow $\bar{v} - c$ are perpendicular (purely crosswise vorticity). The peak draws up loops of vortex lines (shown slightly above, instead of in, the surface for clarity), giving rise to cyclonic vorticity on the right side of the peak (relative to shear vector S) and anticyclonic vorticity on the left side. [Solenoidal effects (not included in drawing) actually divert the vortex lines around the right (left) side of a warm (cool) peak, relative to the mean vorticity vector, but do not alter the result.] Environmental flow across expanding peak produces maximum updraft upstream (storm-relative frame) of peak due to upslope component of vertical velocity. In this case, there is no correlation between vertical velocity and vertical vorticity since centers of w'-field lie in different quadrants of peak from those of ζ'-field.

Davies-Jones 1984

FIG. 8. As in Fig. 7, but for other extreme when vorticity is purely streamwise (i.e., ω is parallel to $\bar{v} - c$). Here, the upslope (downslope) side of the peak is also the cyclonic (anticyclonic) side, and vertical velocity and vertical vorticity are positively correlated.
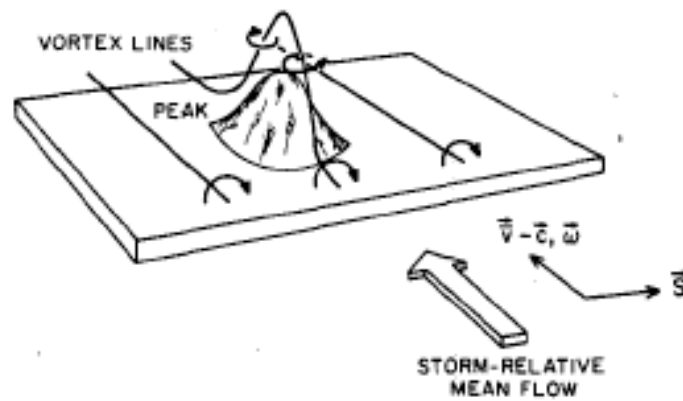
Davies-Jones 1984

BELTRAMI FORCING Z = 3.0 km T = 40 MIN

FIG. 17. Magnitude of the components of the Bernoulli and Lamb vector terms in the momentum equation at 3 km AGL at 40 min for the (a), (b) straight shear, (c), (d) quarter-circle shear, and (e), (f) half-circle shear simulations, respectively, as described in the text. The horizontal components are plotted as horizontal vectors, with a vector length of one grid interval equal to a magnitude of 0.15 m s^{-2}. The vertical component is contoured at 0.02 m s^{-2} intervals, with the zero contour omitted. The sum of the two vertical components is essentially equivalent to the full vertical dynamic pressure gradient forcing (PZDN), as presented in Figs. 10–12. The updraft region is cross hatched, with the dark and light hatching representing vertical velocities between 4 and 14 m s^{-1}, and greater than 14 m s^{-1}, respectively. The full domain has been windowed to a 20 km by 20 km region, centered on the moving storms. Tick marks are included every km.

Weisman and Rotunno 2000

BELTRAMI FORCING Z = 3.0 km T = 40 MIN

(a) FULL CIRCLE   PZBN (b) FULL CIRCLE   PZLA
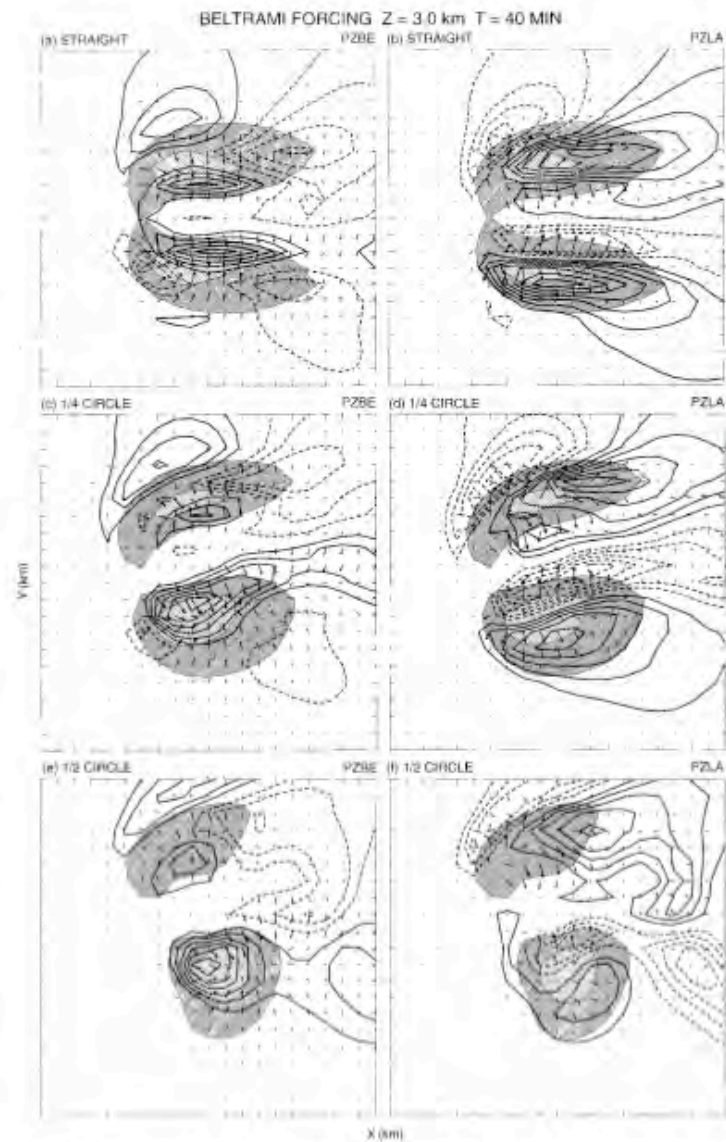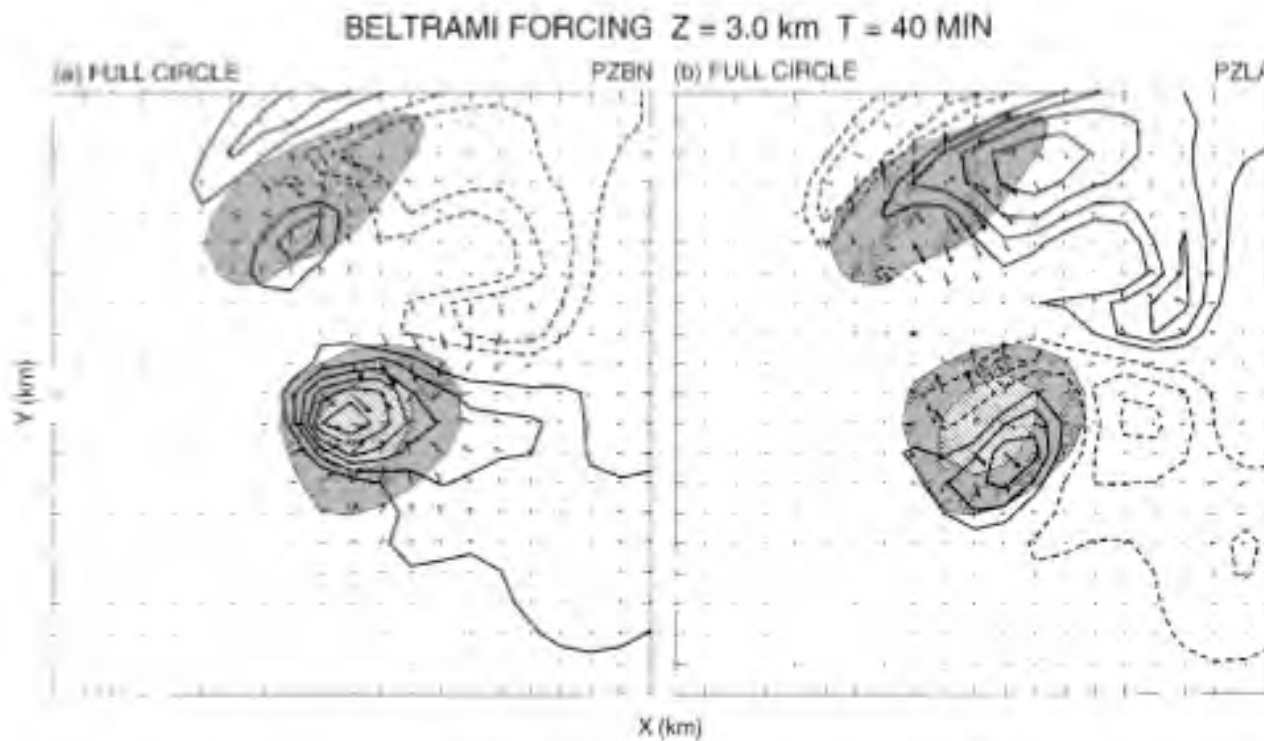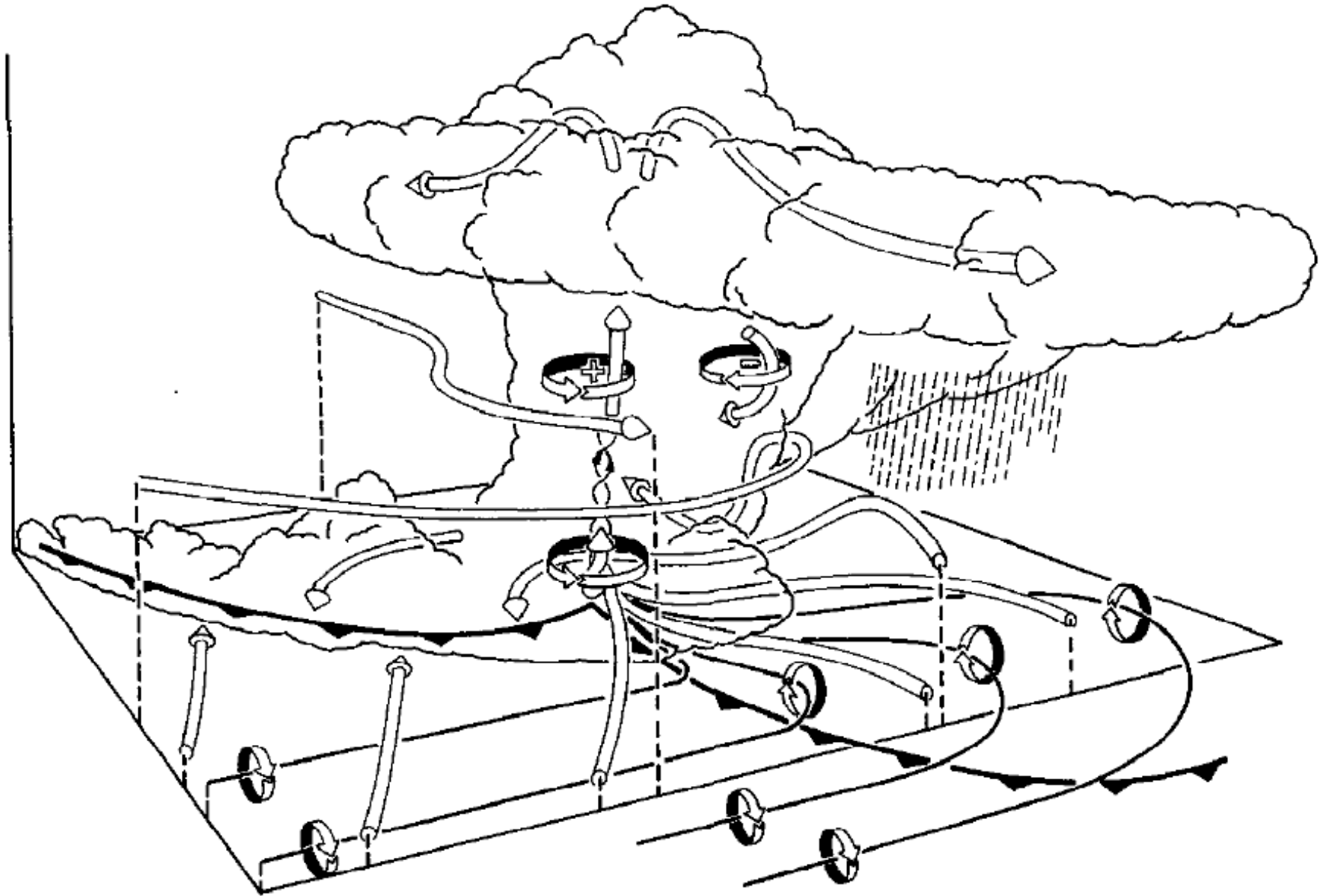
FIG. 18. Magnitude of the components of the (a) Bernoulli and (b) Lamb vector terms in the momentum equation at 3 km AGL at 40 min for the full-circle shear simulation, as described for Fig. 17.

Weisman and Rotunno 2000

PRODUCTION OF LOW-LEVEL MESOCYCLONE

Klemp 1987

REAR-FLANK
DOWNDRAFT

"VORTEX-VALVE
EFFECT"

Klemp 1987
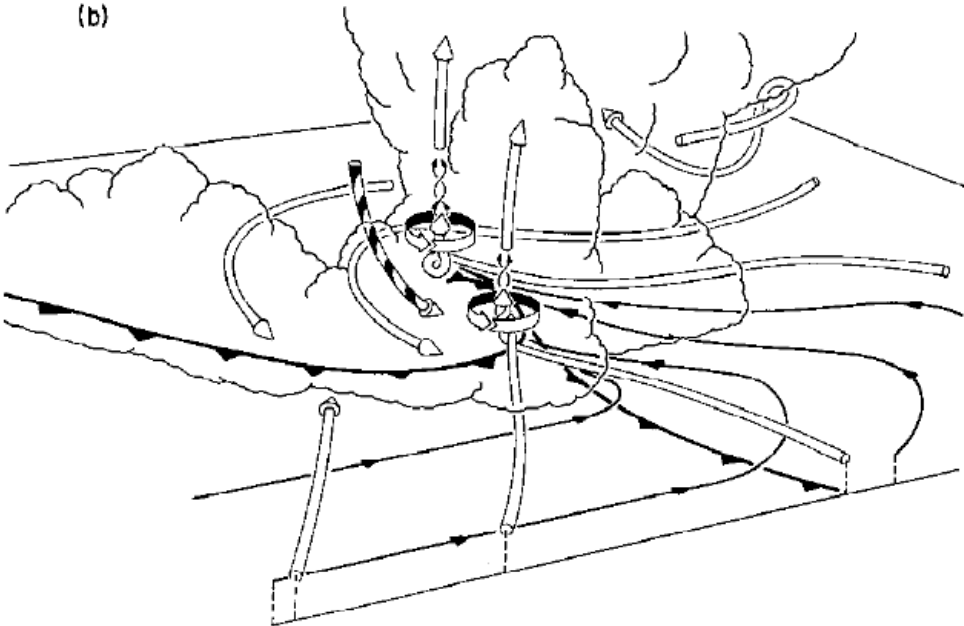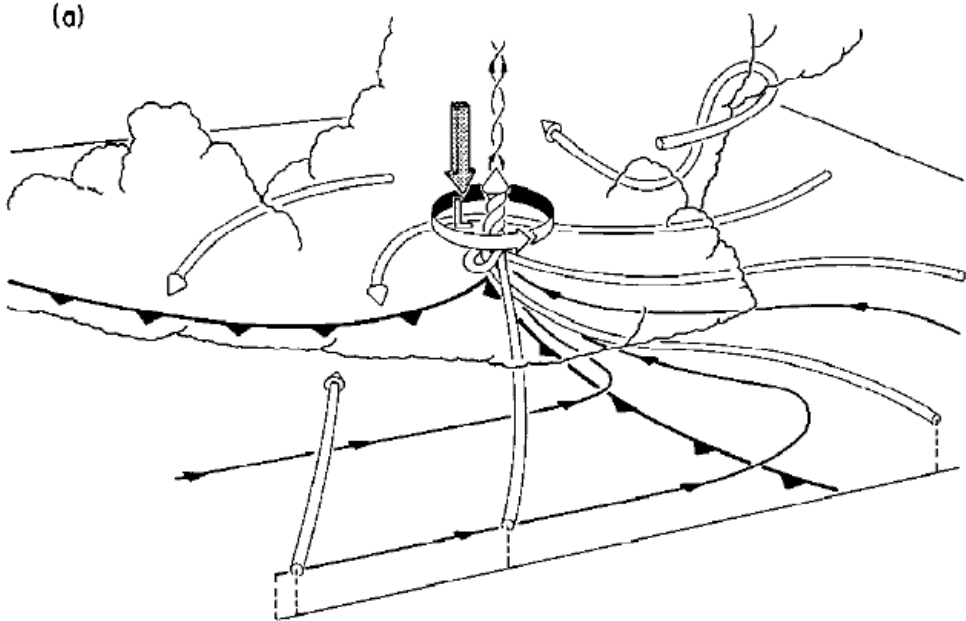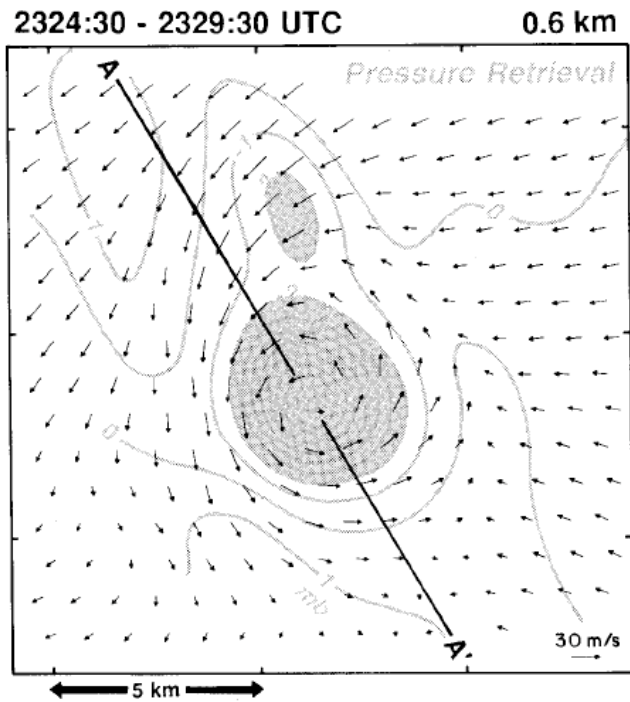
FIG. 11. Retrieved perturbation pressure at 2324:30–2329:30 UTC superimposed onto the wind field at 600 m. Isobars are drawn as gray lines with values less than −2 mb shaded gray. The black line denotes the location of a vertical cross section shown in Fig. 12.
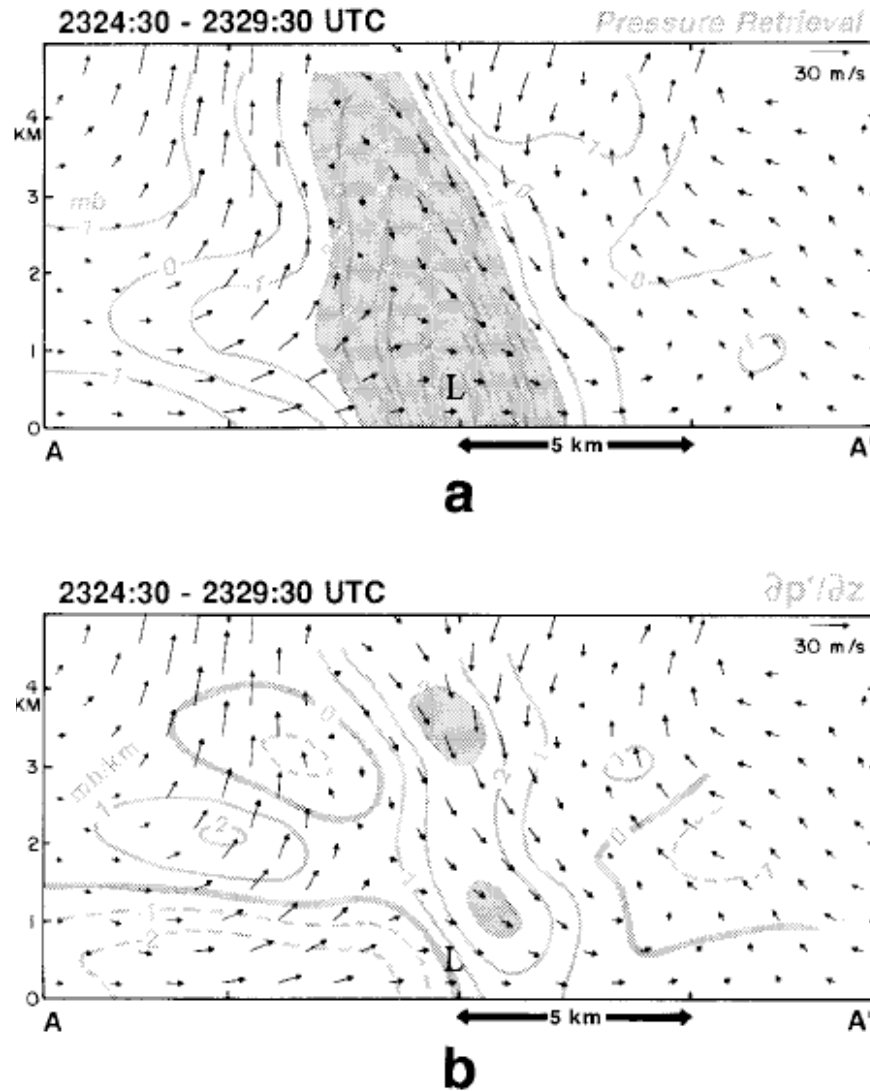
FIG. 12. Vertical cross section depicting the wind field superimposed onto (a) the isobars through the mesolow, and (b) the vertical pressure gradient. Isobars are drawn as gray lines with values less than −2 mb shaded gray. Positive and negative isopleths of constant pressure gradient are drawn as gray and dashed gray lines with values greater than 3 mb km^{-1} shaded gray. The location of the cross section is shown by the black line in Fig. 11.

Garden City, KS
Storm
16 May 1995

Wakimoto et al. 1998
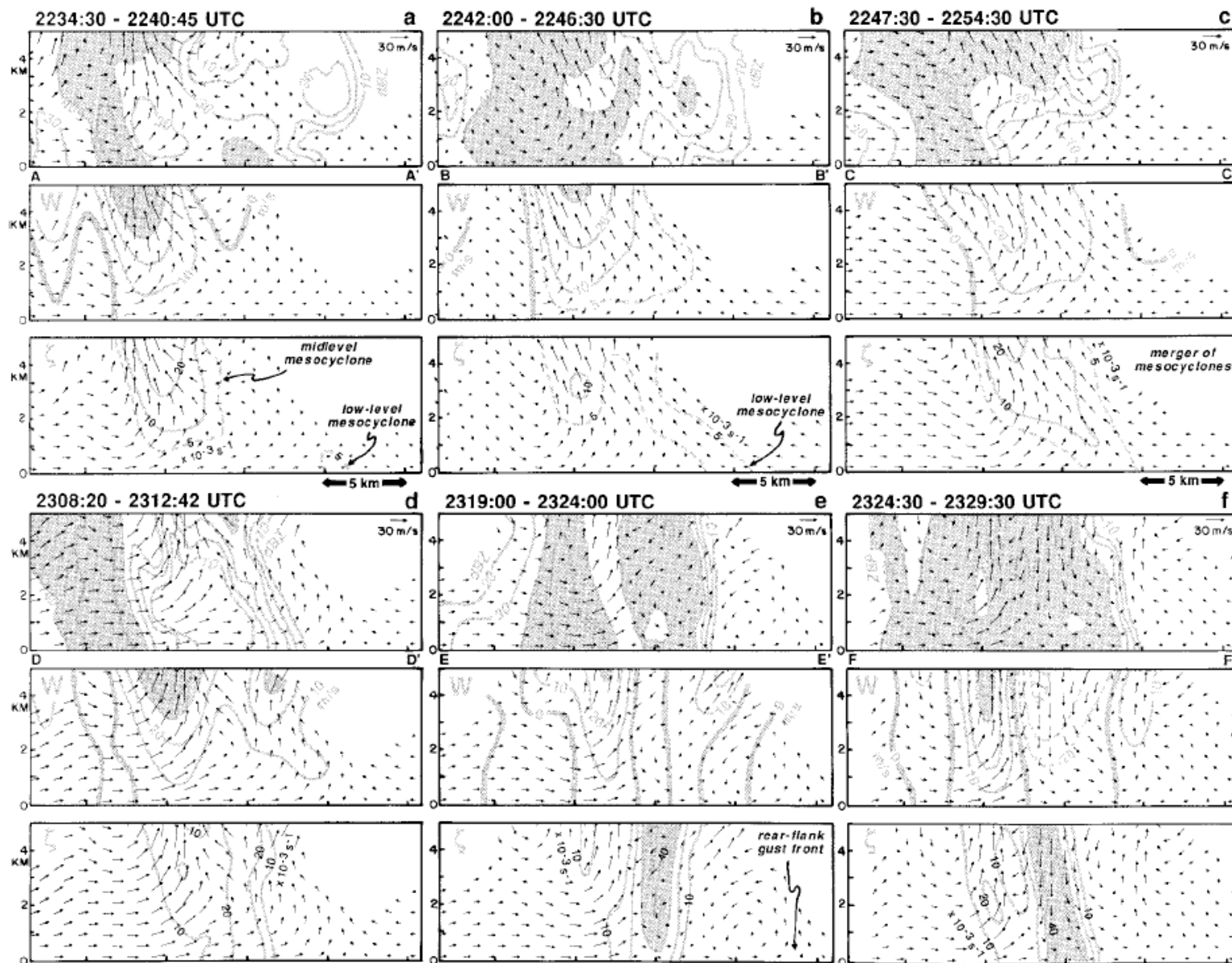
FIG. 10. Vertical cross sections of radar reflectivity, vertical velocity, and vertical vorticity through the low-level and midlevel mesocyclones at (a) 2234:30–2240:45, (b) 2242:00–2246:30, (c) 2247:30–2254:30, (d) 2308:20–2312:42, (e) 2319:00–2324:00, and (f) 2324:30–2329:30 UTC. Locations of vertical cross sections are shown in Fig. 5. Radar reflectivity are drawn as gray lines with values greater than 40 dBZ shaded gray. Positive and negative values of vertical velocity and vorticity are drawn as gray lines and dashed gray lines, respectively. Vorticity and velocity values greater than 30×10^{-3} s^{-1} and 30 m s^{-1} are shaded gray. Vertical velocities less than -30 m s^{-1} are hatched.

Wakimoto et al. 1998

FIG. 14. A schematic model summarizing the life cycle of the Garden City storm. Cylindrical arrows depict the storm-relative flow. The location of the low-level and midlevel vorticity centers is shown by the ribbon arrows. The synoptic-scale trough is shown by the black dashed line. The rear- and forward-flank gust fronts are indicated by the frontal symbols. The occlusion downdraft is shown by the black arrow.

Browning and Landry
1963 Radar Conf.
(no figure)

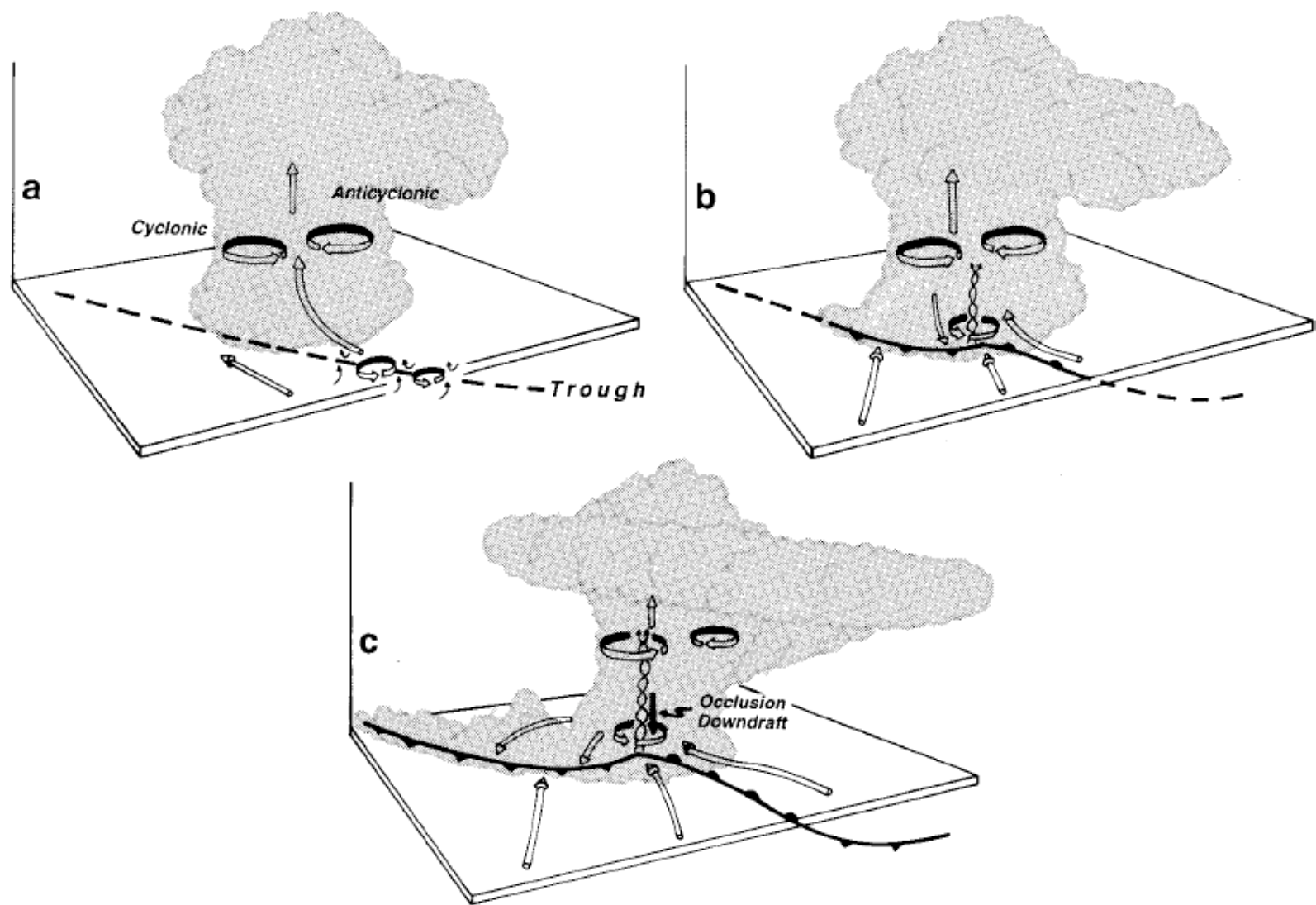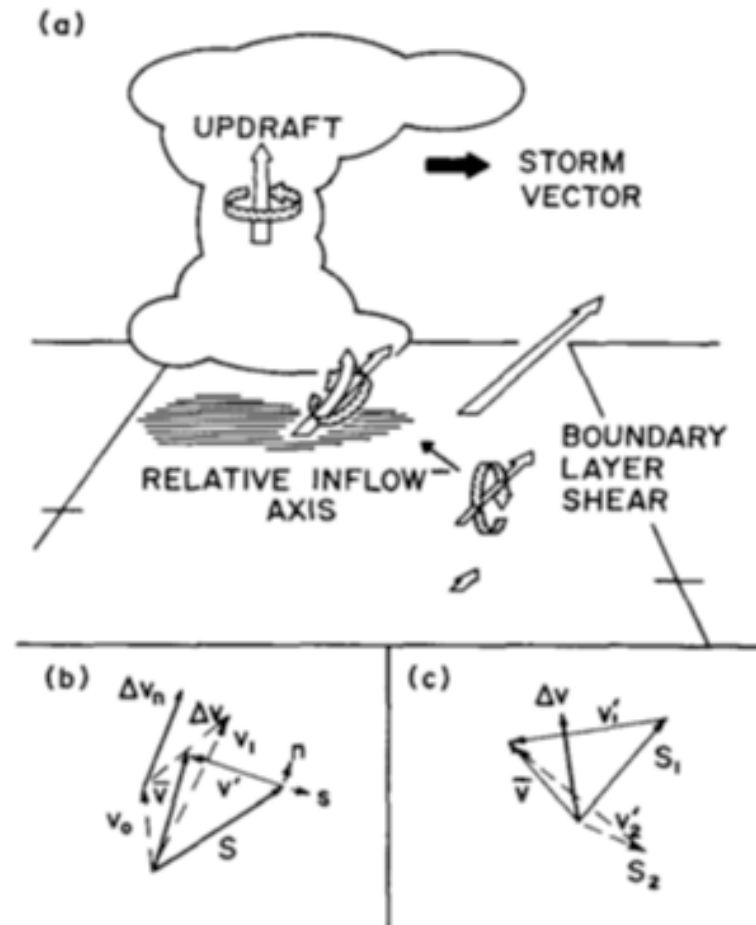FIG. 16. (a) Schematic of process which generates vorticity about vertical axis of updraft from shear in boundary layer for a thunderstorm moving across the low-level wind field (after Barnes, 1968). (b) Relationship of vectors which influence $\partial v_n/\partial s$ in the tilting term. Relative inflow vector v' is determined by storm vector S and mean wind $\bar{v}$ in boundary layer. Boundary layer shear Δv is vector difference between surface wind v_0 and wind at ~ 1 km. Only the component of shear normal to the inflow vector Δv_n contributes significantly to the tilting term. (c) Vector relationships corresponding to the numerical values in Tables 3 and 4 used to estimate tilting term. Subscripts indicate times prior to and after 1700.

Barnes 1970

(a)

supercell with mid-level rotation or non-supercell with no rotation

BAROCLINIC ZONE

BAROCLINIC ZONE

too cold, deep, and stable air mass

sloping zone of enhanced horizontal vorticity - cooler, but sufficiently conditionally unstable

warm, conditionally unstable air mass

(b)

inflow trajectory

rapid low-level mesocyclogenesis

(c)

weakening storm and / or weakening low-level rotation

cold, stable air

Markowski et al. 1998a

Fig. 2. A conceptual model for how an updraft-boundary interaction may lead to low-level mesocyclogenesis.

Storm-Relative Trajectories Through Anvil-Generated Baroclinity

N
E

Updraft

baroclinic horizontal vorticity generation zone

Storm-relative inflow trajectory

8 June 1995

Updraft

baroclinic horizontal vorticity generation zone

Storm-relative inflow trajectory

22 May 1995

Updraft

baroclinic horizontal vorticity generation zone

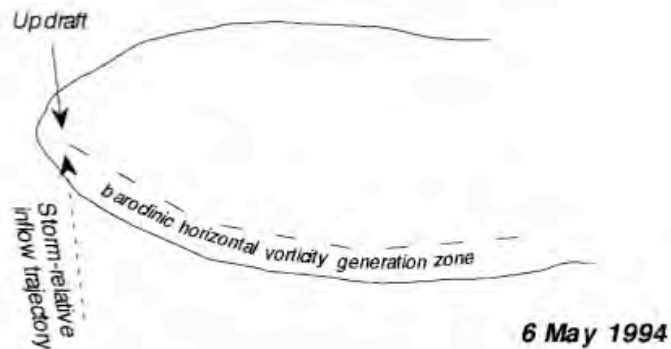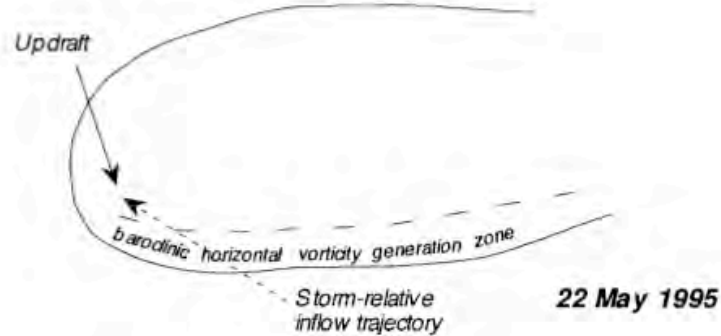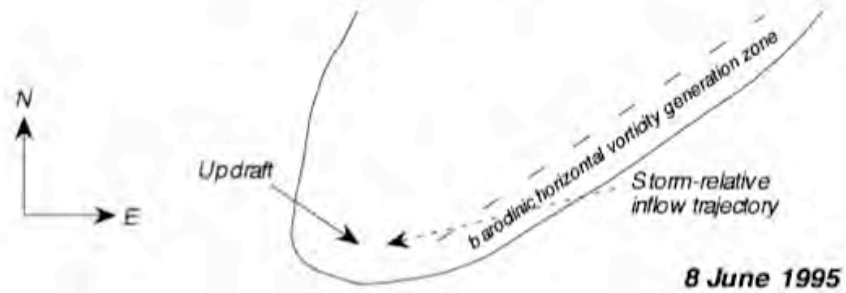Storm-relative inflow trajectory

6 May 1994

FIG. 17. Schematic representation of the storm-relative trajectories through the anvil-generated baroclinic zones on 8 June 1995, 22 May 1995, and 6 May 1994. In the first two cases, not only does the vorticity generated contain a greater streamwise component, but the parcel residence times in the baroclinity are longer. See Figs. 16a,b for examples of hodographs that would favor the first two scenarios for extended baroclinic vorticity generation, and Fig. 16c for an example of a hodograph that would not provide a favorable storm-relative flow for long parcel residence times in anvil-generated baroclinity.
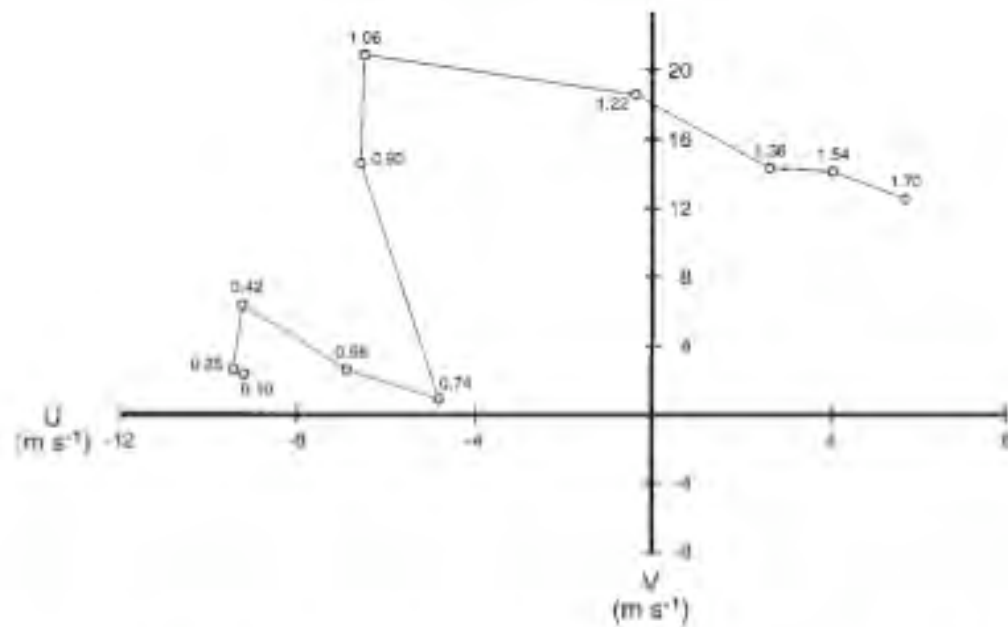
Markowski et al. 1998

FIG. 7. Hodograph constructed from VAD data collected by the radar (see the text for details) approximately 1838 CDT 15 May 1999, 6.1 km north of Plainville, KS. Heights shown are in km AGL.
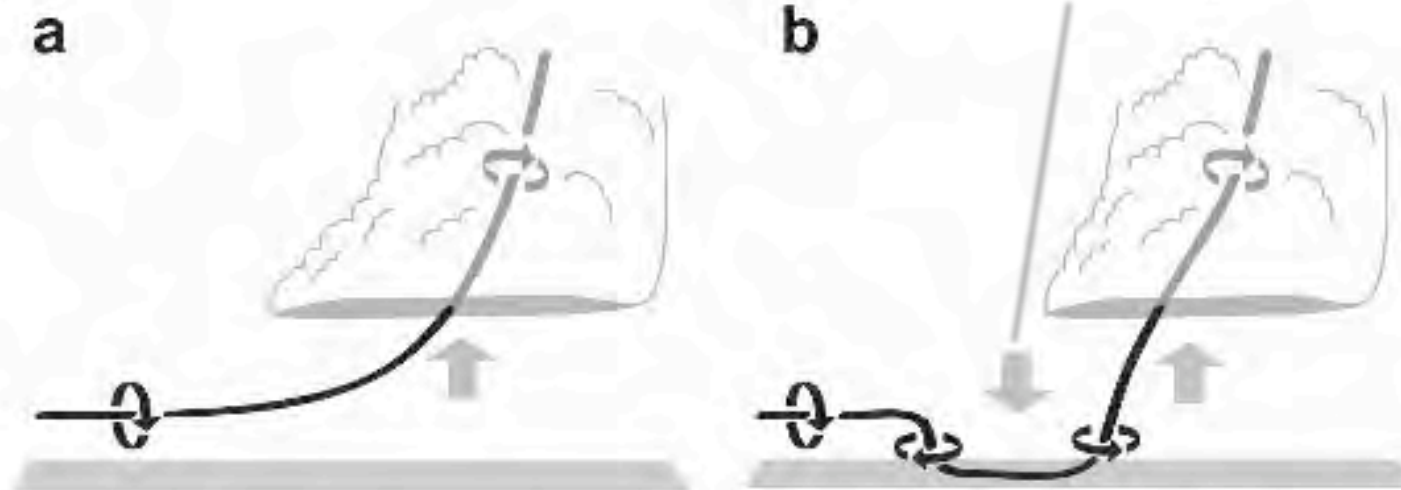
Bluestein and Pazmany 2000

Fig. 16. (a) Tilting of ambient (barotropic) horizontal vorticity by an updraft produces midlevel vertical vorticity. In the above case, the ambient horizontal vorticity has a significant streamwise component so that the midlevel vertical vorticity maximum lies within the updraft. Vertical vorticity cannot arise next to the ground because air is rising away from the ground as vertical vorticity is being generated by the tilting effect. (b) If a downdraft develops, vertical vorticity can be advected toward the surface as it is produced via tilting, resulting in significant vertical vorticity next to the ground. If baroclinity is absent (and turbulent diffusion is neglected), vortex lines are frozen in the fluid and are redistributed by the downdraft as material lines. In this case, the vortex line passing through the low-level vertical vorticity maximum takes a U shape rather than an arch. A couplet of counterrotating vortices straddles the downdraft maximum. Of course, the very presence of a downdraft implies that at least some solenoidal effects are unavoidable, even if the downdraft is driven solely by dynamic pressure perturbations. Just as the presence of a warm isentropic peak in Fig. 1 actually diverts vortex lines toward the right as the lines are lifted by the peak (refer to the Fig. 1 caption), vortex lines would actually be diverted toward the left (i.e., in the opposite direction) in the case above. This is not easily shown in the figure above, nor does it dramatically alter the main result, which is a U-shaped vortex line at low levels.
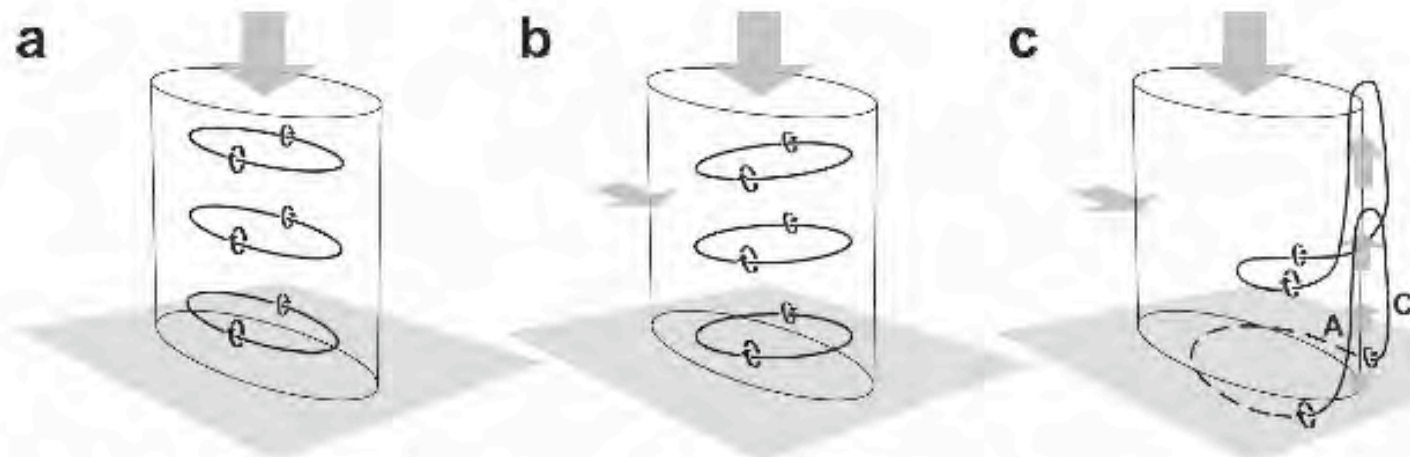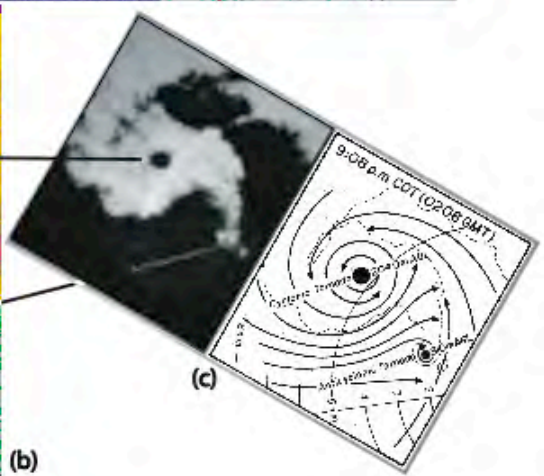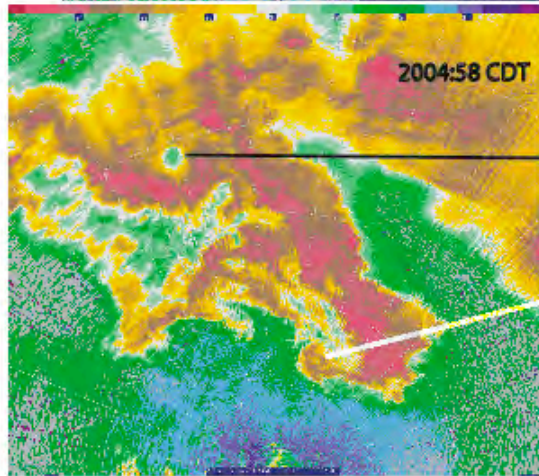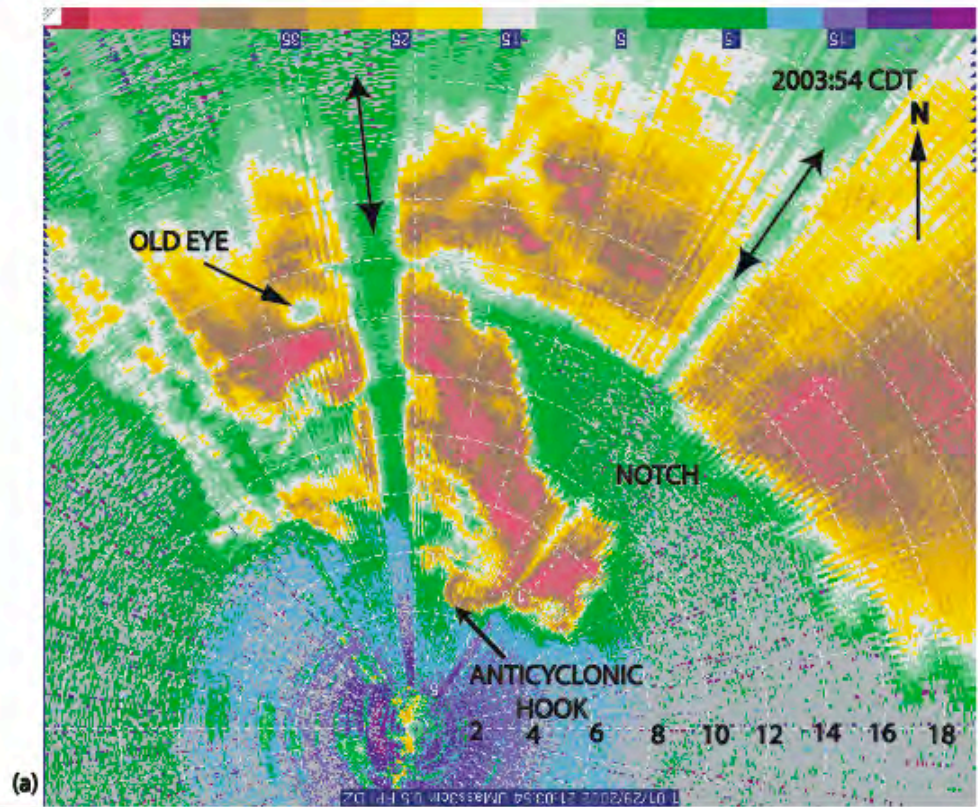
Markowski et al. 2008

FIG. 17. One possible way by which a couplet of vertical vorticity can be produced by a purely baroclinic process in an environment containing no ambient vorticity (neither vertical nor horizontal). (a) Baroclinically generated vortex rings encircle a buoyancy minimum that extends throughout a vertical column (such a region of negative buoyancy might be found in the hook echo/RFD region of a supercell, for example); the presence of negative buoyancy causes the rings to sink toward the ground as they are generated. (b) If the vortex rings are swept forward as they descend toward the ground owing to the additional presence of rear-to-front flow through the buoyancy minimum, the vortex rings become tilted upward on their downstream sides (a vertical velocity gradient is present within the column because buoyancy is a minimum in the center of the column and increases with increasing distance from the center of the column). (c) If the leading edge of the vortex rings can be lifted by an updraft in close proximity to the buoyancy minimum (an updraft is typically found in close proximity to the hook echo/RFD region of a supercell, for example), then the vortex rings can be tilted further and stretched upward, leading to arching vortex lines and a couplet of cyclonic ("C") and anticyclonic ("A") vertical vorticity that straddles the buoyancy minimum and associated downdraft. Note the similarity to Fig. 15. (Adapted from Straka et al. 2007.)

Markowski et al. 2008

(a)

2003:54 CDT

N

OLD EYE

NOTCH

ANTICYCLONIC HOOK

2 4 6 8 10 12 14 16 18

(b)

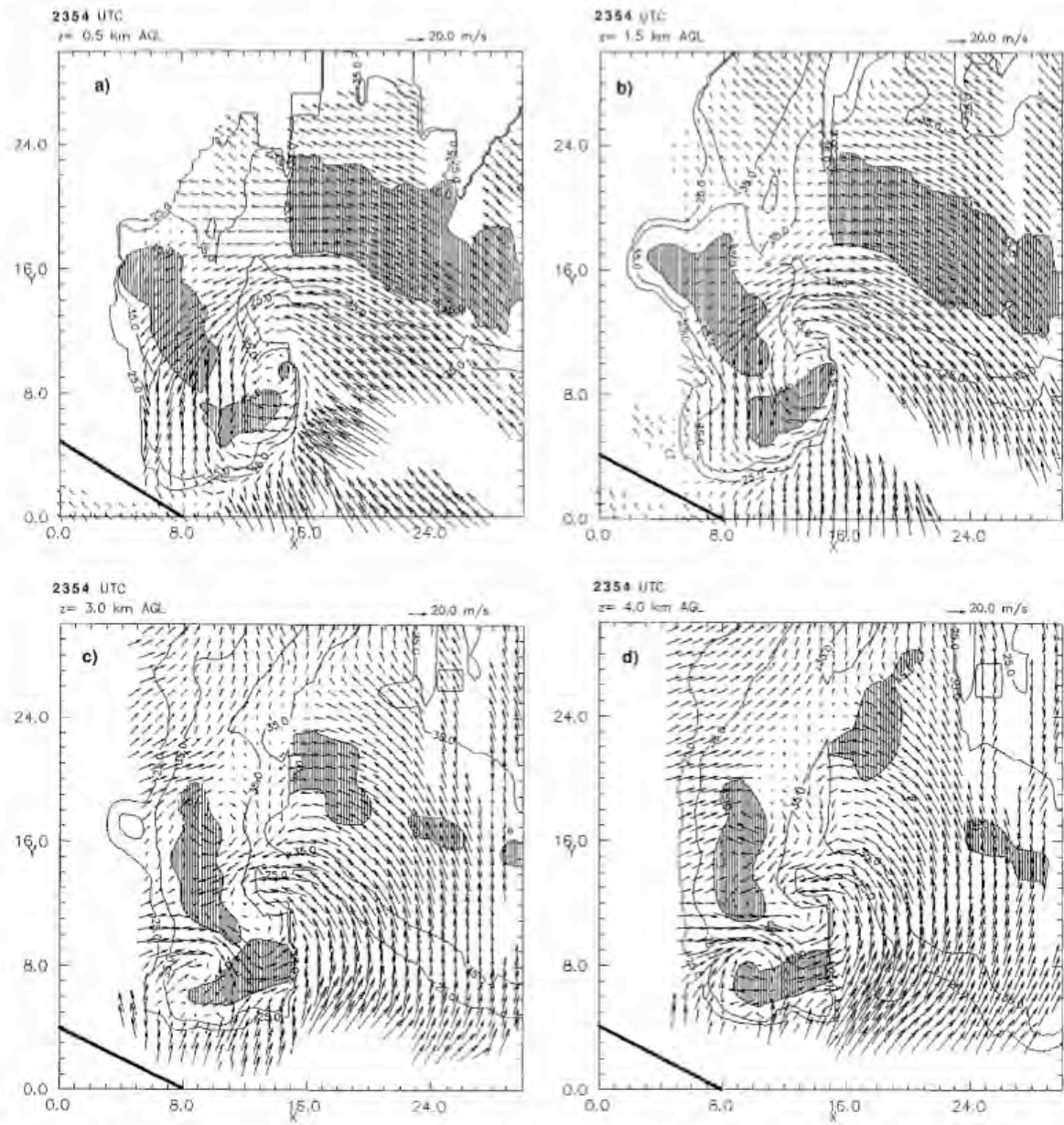2004:58 CDT

(c)

9:08 a.m. CDT (02G8.9MT)

FIG. 9. Radar reflectivity factor and synthesized storm-relative horizontal winds at 2354 UTC on 22 May 1995 at (a) 0.5, (b) 1.5, (c) 3.0, and (d) 4.0 km AGL. The scale for the vectors is shown at the upper right of each panel. Areas of reflectivity greater than 45 dBZ are shaded. Minor (major) tick marks are shown every 1 (8) km. Sharp reflectivity gradients at approximately x = 15 km are due to brief (~10 s) lapses in data from ELDORA. There is still, however, a strong gradient of reflectivity in these regions, as confirmed by the Amarillo WSR-88D (not shown); this analysis has overly sharpened that gradient. The effect of these missing data on the velocity fields is minimal. The approximate ESE flight track is indicated by a solid line at the lower left of each panel.
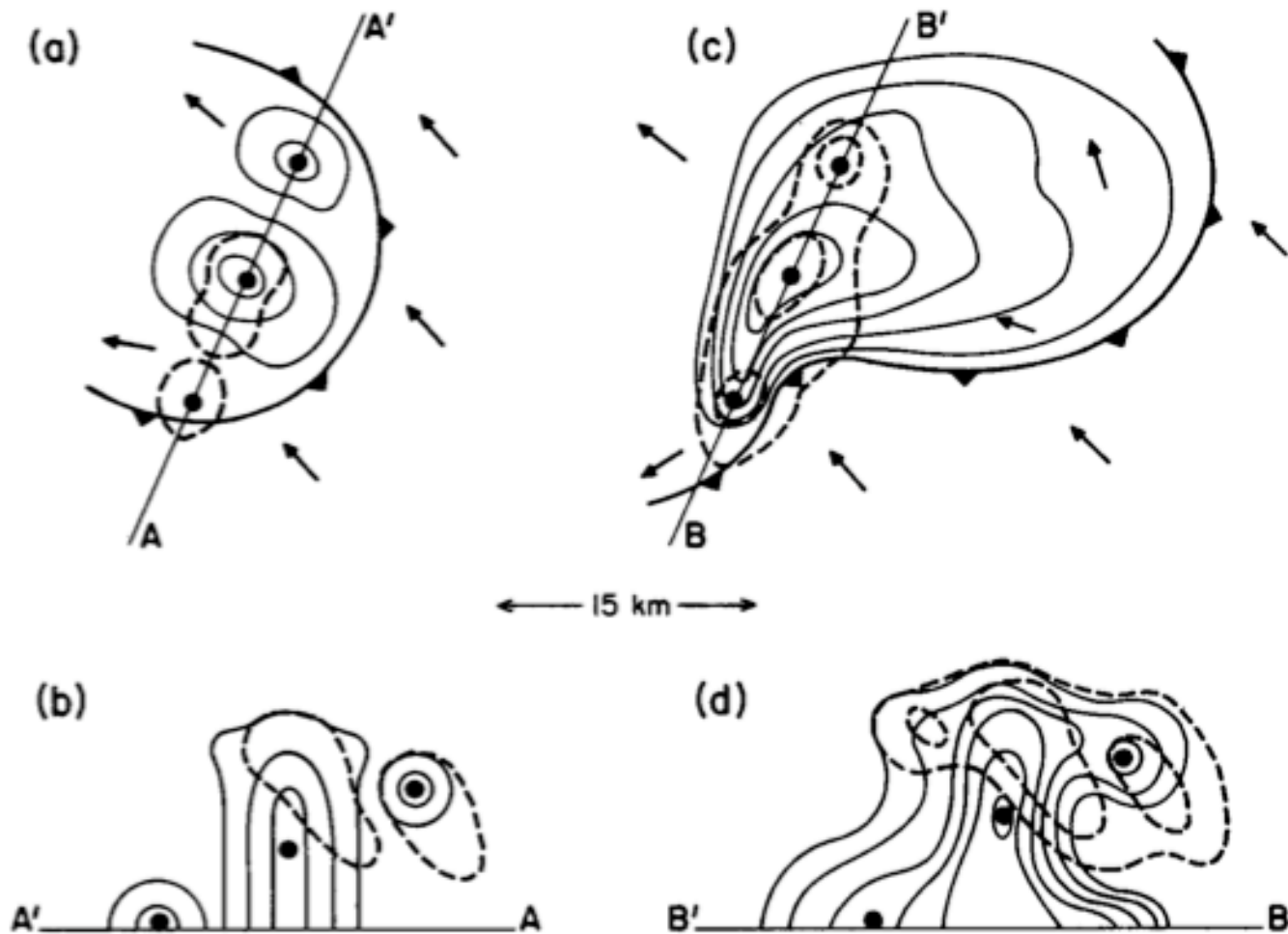
Bluestein and Gaddy 2001

FIG. 17. Schematic diagrams, derived from observations, representing a conceptual model of storm structure: (a) plan view during multicell phase; (b) vertical section during multicell phase; (c) plan view during supercell phase; (d) vertical section during supercell phase. Solid contours are reflectivity [low-level in (a) and (c)] at 10-dBZ intervals. Dashed lines indicate updraft at 10 m s⁻¹ intervals, beginning with 10 m s⁻¹, at middle to upper levels. Large dots indicate the projection of reflectivity maxima at any level. The barbed lines in (a) and (c) depict the gust front, and arrows represent the storm-relative, low-level airflow. Note that the cell separation is the same during both multicell and supercell phases.

Vasiloff et al. 1986